Biochemistry **1995**, *34*, 16733–16752

Frequency Spectrum of NH Bonds in Eglin c from Spectral Density Mapping at Multiple Fields[†]

Jeffrey W. Peng[‡] and Gerhard Wagner*[,§]

Vertex Pharmaceuticals, Inc., 40 Allston Street, Cambridge, Massachusetts 02139, and Department of Biological Chemistry and Molecular Pharmacology, Harvard Medical School, Boston, Massachusetts 02115

Received August 10, 1995; Revised Manuscript Received October 12, 1995[⊗]

ABSTRACT: The internal mobility of the protein eglin c is characterized with spectral density functions of the NH vectors obtained from heteronuclear NMR relaxation at multiple field strengths (7.04, 11.74, and 14.1 T). The spectral density functions, $J(\omega)$, describe the frequency spectrum of the rotational fluctuations of the XH bond vectors ($^{15}N-^{1}H$ and $^{13}C-^{1}H$). The spectral density-mapping approach [Peng, J. W., & Wagner, G. (1992a) *J. Magn. Reson. 98*, 308–332; Peng, J. W., & Wagner, G. (1992b) *Biochemistry 31*, 8571–8586] permits the direct evaluation of $J(\omega)$ at the five frequencies 0, ω_N, $|\omega_H| - |\omega_X|$, ω_H, and $|\omega_H| + |\omega_X|$. The $^{15}N-^{1}H$ relaxation measurements from three field strengths on ^{15}N-enriched eglin c resulted in 18 relaxation rate constants per NH bond and 13 unique evaluations of each NH spectral density function. Dynamic heterogeneity along the protein backbone is manifested most clearly in spectral density values at lower frequencies (<100 MHz). The effective value of $J(0)$, $J_{\mathrm{eff}}(0)$, is the most sensitive probe of dynamics as it is affected by both rapid internal motions and slow chemical exchange processes. Low $J_{\mathrm{eff}}(0)$ and $J(\omega_N)$ values are correlated with fast amide proton–deuteron exchange rates; the converse, however, is not observed. Anomalies in $J(\omega_H)$ and $J(|\omega_H|\pm|\omega_N|)$ observed in the first applications of the spectral-mapping approach are now attributable to the high sensitivity of these values to small errors in the rate constants. These anomalies can be reduced by the use of a reduced spectral-mapping procedure. The use of multiple field strengths allows the identification of slow exchange processes manifested as an increase of $J_{\mathrm{eff}}(0)$ with spectrometer field strength.

The study of the relationship between protein dynamics and protein function is drawing increasing scrutiny by both experimental and theoretical approaches. A particularly powerful experimental approach has been the measurement of heteronuclear nuclear magnetic resonance (NMR)[1] relaxation rates. Examples of such measurements include the measurement of spin lattice and spin–spin relaxation rate measurements for XH bonds, such as $^{15}N-^{1}H$ or $^{13}C-^{1}H$ spin systems in the protein. Current two-dimensional (2D) heteronuclear pulsed NMR methods permit dynamic information to be extracted from virtually all NH bonds along the protein backbone (Nirmala & Wagner, 1988, 1989; Kay et al., 1989). Recently, a large number of such heteronuclear relaxation measurements have focused on amide $^{15}N-^{1}H$ spin systems in isotopically enriched protein samples, thereby allowing the local dynamics along the protein backbone to be explored. Such relaxation studies have been able to identify regions of enhanced internal flexibility (Kay et al., 1989; Clore et al., 1990a,b; Kelsh et al., 1992; Kördel et al., 1992; Schneider et al., 1992; Barbato et al., 1992; Stone et al., 1992; Redfield et al., 1992; Peng & Wagner, 1992a,b; Powers et al., 1992; Szyperski et al., 1993; Cheng et al., 1993, 1994; Akke et al., 1993; Nicholson et al., 1995). In some cases, these regions are associated with those portions of the backbone directly involved in the active site [e.g. Heinz et al. (1992), Akke et al. (1993), and Nicholson et al. (1995)].

The dynamic information content of the heteronuclear relaxation rate constants consists of discrete evaluations of the spectral density functions belonging to the various XH bonds. The spectral densities are typically denoted by $J(\omega)$ and correspond to the power spectra pertaining to the orientational fluctuations of XH bond vectors relative to the external field, $\mathbf{B}_o$. Recently, we have proposed a strategy in which one measures a set of six relaxation parameters for the XH bonds at a given B_o field strength (Peng & Wagner, 1992a,b). Such measurements provide the necessary information for the direct yield of the spectral density values from experiment and thereby "map" the spectral density functions for each XH bond. This contrasts with approaches in which model forms of the spectral density are used to interpret the NMR relaxation rate constants. In such model-based approaches, the dynamics conclusions depend upon both the accuracy of the NMR experiments and the inherent assumptions of the model. In contrast, the verity of the dynamics information in the spectral density-mapping approach depends only upon the accuracy of the NMR experiments.

We have previously applied this new strategy to amide $^{15}N-^{1}H$ spin systems in a small proteinase inhibitor, eglin c, in order to characterize the backbone flexibility of the protein (Peng & Wagner, 1992a,b). The results of this study were spectral density values at frequencies including 0, 50, 450, 500, and 550 MHz. This sampling of the $J(\omega)$ values was rather sparse, due to the fact the relaxation rates were

---

[†] This work was supported by the NSF (Grant MCB 9316938) and the Keck Foundation.

* Author to whom correspondence should be addressed.

[‡] Vertex Pharmaceuticals, Inc.

[§] Harvard Medical School.

[⊗] Abstract published in *Advance ACS Abstracts*, December 1, 1995.

[1] Abbreviations: CSA, chemical shift anisotropy; CW, continuous wave; DD, dipole–dipole; FID, free induction decay; HSQC, heteronuclear single quantum coherence spectroscopy; INEPT, insensitive nuclei enhancement by polarization transfer; NMR, nuclear magnetic resonance; NOE, nuclear Overhauser effect; rf, radio frequency; TPPI, time proportional phase incrementation.

0006-2960/95/0434-16733$09.00/0

recorded only at a single field strength (11.74 T). Additionally, anomalous behavior for some of the spectral density values at 450, 500, and 550 MHz was observed in the form of slight increases, or even negative values.

Acknowledging this, we have endeavored here to construct a more detailed picture of the spectral density functions for eglin c, using relaxation rates at 7.04 and 14.1 T to complement the previous results from 11.74 T. Eglin c is a 70-residue inhibitor (molecular mass = 8 kDa) that binds to such proteases as elastase, subtilisin, thermistase, and chymotrypsin. The crystal structure of eglin c in complex with subtilisin Carlsberg has been determined (McPhalen et al., 1985; Bode et al., 1986, 1987). The crystal structure of free eglin c (Hipler et al., 1992) and the solution structure of free eglin c have been elucidated as well (Hyberts et al., 1992). The relaxation data from the three field strengths gives 13 unique sampling points of each $^{15}N-^{1}H$ $J(\omega)$ function. The result is a clearer view of the shape of the spectral density functions and a thorough investigation of the practical aspects of using the spectral density-mapping approach. The results also show that spectral density mapping at multiple field strengths provides a sensitive tool for identifying slow chemical exchange processes.

MATERIALS AND METHODS

NMR Spectroscopy. Following the experimental strategy outlined previously (Peng & Wagner, 1992a,b), six relaxation rate constants were measured for the $^{15}N-^{1}H$ spin systems of eglin c at three B_0 field strengths, including 7.04 (300 MHz ^1H frequency), 11.74 (500 MHz ^1H frequency), and 14.1 T (600 MHz ^1H frequency). The rate constants include $R_N(N_z)$, the rate constant for longitudinal ^{15}N magnetization $\langle N_z\rangle$ relaxation, $R_N(N_x)$, the rate constant for in-phase ^{15}N single quantum coherence $\langle N_x\rangle$ relaxation, $R_{HN}(2H_z^N N_x)$, the rate constant for antiphase ^{15}N single quantum coherence $\langle 2H_z^N N_x\rangle$ relaxation, $R_{HN}(2H_z^N N_z)$, the rate constant for longitudinal heteronuclear two-spin order $\langle 2H_z^N N_z\rangle$ relaxation, $R_H(H_z^N)$, the rate constant for amide proton longitudinal $\langle H_z^N\rangle$ relaxation, and $R_N(H_z^N \leftrightarrow N_z)$, which denotes the rate constant for longitudinal cross-relaxation between $\langle H_z^N\rangle$ and $\langle N_z\rangle$.

The same degassed 3.8 mM sample of uniformly ^{15}N-enriched eglin c was used for all experiments at all field strengths. Experiments were performed at 36 °C and pH $\approx$ 3.0 using Bruker AMX300, AMX500, and AMX600 spectrometers. The relaxation pulse sequences were based on 2D $^{15}N-^{1}H$ heteronuclear correlation sequences using INEPT polarization transfers; details of these experiments are discussed elsewhere (Kay et al., 1989; Peng & Wagner, 1992a,b, 1994a,b). Note that these sequences used water presaturation and may therefore result in small underestimates of the heteronuclear NOE. The use of more recently developed gradient versions of these relaxation experiments can circumvent these problems (Dayie & Wagner, 1994). The strength of the CW ^{15}N spin lock for the $R_N(N_x)$ and $R_{HN}(2H_z^N N_x)$ measurements was 2500 Hz. To measure these rates for the upfield arginine ϵ-side chains, the carrier was repositioned to minimize resonance offset effects. Each 2D spectra consisted of 128 increments in the ^{15}N dimensions, with 2048 complex points per FID. Quadrature detection in t_1 was obtained via the TPPI method of Marion and Wüthrich (1983). The relaxation data sets were recorded with the following relaxation delay times. Longitudinal ^{15}N relaxation rate $R_N(N_z)$ used delays of 10, 10, 50, 100, 150, 200, 300, 400, 800, and 2000 ms at 300 MHz; 10, 50, 100, 150, 200, 300, 400, 500, 800, 2000, and 3000 ms at 500 MHz; and 10, 50, 100, 150, 200, 325, 450, 650, 850, 1000, 2000, and 3000 ms at 600 MHz. In-phase transverse relaxation rate $R_N(N_x)$ measurements included delays of 6.4, 25.6, 25.6, 38.4, 51.2, 76.8, 102.4, 128.0, and 153.6 ms at 300 MHz; 6.4, 6.4, 12.8, 25.6, 38.4, 51.2, 76.8, 102.4, 140.8, and 179.2 ms at 500 MHz; and 12.8, 25.7, 25.7, 38.5, 51.4, 77.1, 102.7, 128.4, and 167 ms at 600 MHz. Antiphase transverse relaxation $R_{HN}(2H_z^N N_x)$ measurements used delays of 6.4, 12.8, 25.6, 25.6, 38.4, 51.2, 76.8, 96, 115.2, and 147.2 ms at 300 MHz; 6.4, 12.8, 25.6, 51.0, 76.0, 102.4, 134.0, and 172.8 ms at 500 MHz; and 3.2, 6.4, 12.8, 25.6, 38.4, 51.2, 76.8, 102.4, and 134.4 ms at 600 MHz. Measurements of the longitudinal two-spin order, $R_{HN}(2H_z^N N_z)$, used delays of 4, 10, 10, 20, 30, 50, 80, 100, 120, and 150 ms at 300 MHz; 2, 10, 20, 30, 50, 70, 100, 130, and 170 ms at 500 MHz; and 2, 10, 20, 20, 40, 60, 80, 100, 140, and 170 ms at 600 MHz. Amide proton spin−lattice relaxation rate measurements $R_H(H_z^N)$ included delays of 10, 10, 20, 30, 40, 60, 80, 100, and 125 ms at 300 MHz; 0.001, 10, 10, 20, 30, 40, 50, 70, 100, and 125 ms at 500 MHz; and 1, 10, 10, 20, 40, 50, 70, 100, and 125 ms at 600 MHz. Heteronuclear cross-relaxation rates require recording of steady-state NOE intensities. At all field strengths, two pairs of spectra were recorded for the steady-state NOE intensities. One pair involved 3 s of proton saturation to achieve the steady-state intensity, while the other pair consisted of the control spectra with no saturation to obtain the Zeeman intensity. The rate constants $R_N(H_z^N \leftrightarrow N_z)$ were then calculated from the ratio NOE = $(\gamma_H/\gamma_N)[R_N(H_z^N \leftrightarrow N_z)/R_N(N_z)]$.

^{15}N assignments were made using $^{15}NH_4NO_2$ as the reference compound. The assignments were based upon comparisons of 2D $^{15}N-^{1}H$ HSQC correlation spectra (Bodenhausen & Ruben, 1980), followed by an MLEV17 (Bax & Davis, 1985) pulse train for TOCSY (Braunschweiler & Ernst, 1983) mixing, with previously established proton assignments (Hyberts & Wagner, 1990). Amide proton−deuteron exchange rates were measured by recording a series of heteronuclear correlation spectra on protonated eglin c dissolved in D_2O, at the same temperature and pH as the relaxation studies (T = 36 °C and pH = 3.0). A total of 20 HSQC spectra using a two-step phase cycle were recorded over a period of 39 h. Each spectrum required approximately 10 min for acquisition.

Data Reduction. All 2D spectra were processed on Sun SLC and IRIS 4D-35 workstations using FELIX 2.05 software provided by Dr. Dennis Hare (Hare Research, Seattle). Sixty-degree-shifted sine-squared window functions were used prior to Fourier transformation. Free induction decays along t_2 were zero-filled and transformed such that only the NH proton resonances were included in the final spectrum of 1024 real points. Interferograms along t_1 were zero-filled twice to a length of 512 real points. The Levenburg−Marquardt algorithm (Marquardt, 1963; Press et al., 1988) was used to extract the relaxation rate constants, assuming a monoexponential decay for cross-peak intensities in the heteronuclear correlation spectra. Intensities were taken by integration of one-dimensional slices through the cross-peak maxima in the 2D spectra. Error estimates for the rates were obtained using a Monte Carlo procedure described earlier (Peng & Wagner, 1992b). The nonlinear least squares fitting algorithms described previously were used to fit the peak intensities to single exponential functions to extract the relaxation rate constants. Spectral density values were computed from either eqs 9−14 or 22−24 presented in the Results and Discussion. Error estimates for the $J(\omega)$ values were computed using two methods. In the first method, a Monte Carlo procedure was used. Specifically, for each NH bond, the experimental relaxation rate constants and their estimated errors were assumed to be the means and variances of Gaussian distributions. From these distributions, 1000 synthetic relaxation data sets were then generated for each NH bond. Equations 9−14 or 22−24 were then used to convert each synthetic data set into the corresponding set of $J(\omega)$ values. The standard deviations of the resulting ensemble of $J(\omega)$ values were then taken as the estimated uncertainties. In the second method, the uncertainties were estimated using simple error propagation. In particular, if one assumes that the errors in the relaxation rate constants are independent and of a purely statistical nature, then the net error propagated to a particular $J(\omega)$ is then the quadrature-weighted sum derived from either eqs 9−14 or eqs 22−24. The weights are simply the coefficients of the various rate constants in eqs 9−14 and 22−24. The $J(\omega)$ error estimates from the two methods were compared; the larger estimate was always taken as the final quoted error.

Eglin c contains six Pro residues, leaving potentially 64 amide NH vectors for probing the backbone flexibility. However, cross-peak overlap in the heteronuclear correlation spectra hindered accurate determinations of relaxation rate constants for several sets of resonances. These resonances include those of Phe36 and Gly70, as well as those of Tyr56 and Val43 at both 11.74 and 14.1 T. At 7.04 T, residues Val66, Leu37, and Phe55 also became severely overlapped and Ser5 became part of the aggregate cross-peak formed from Val43 and Tyr56. Thus, a common set of 56 NH vectors could be studied free from resonance overlap at all three fields.

RESULTS AND DISCUSSION

Theoretical Background. Only a brief overview of nuclear spin relaxation theory is presented here. More detailed and thorough discussions are available elsewhere (Redfield, 1957; Abragam, 1961; Ernst et al., 1987; Goldman, 1988; Slichter, 1978). Molecular motion has the effect of modulating local field interactions experienced by the ^{15}N and ^{1}H nuclei in the protein. The modulated local fields form the bases for the various relaxation mechanisms which provide the means for the relaxation of nonequilibrium NH spin orders. The rate constants for the relaxation can be expressed in terms of linear combinations of spectral density functions sampled at the various Larmor frequencies of the spin system. The precise linear combination of spectral density functions depends on the type of relaxation mechanism and on the spin order of interest. The primary relaxation mechanisms affecting all NH bonds consist of orientational fluctuations of the NH bond vectors relative to $\mathbf{B}_o$ that modulate the heteronuclear dipole−dipole (DD) interaction and the chemical shift anisotropy (CSA) of the ^{15}N nucleus. Additionally, some NH bonds may participate in exchange processes that modulate the ^{15}N chemical shift; this has the effect of increasing the transverse relaxation rate constants $R_{\mathrm{N}}(\mathrm{N}_x)$ and $R_{\mathrm{HN}}(2\mathrm{H}_z^{\mathrm{N}}\,\mathrm{N}_x)$. If the spectral density functions for the NH orientational fluctuations are denoted as $J(\omega)$, the six relaxation rates listed in the Materials and Methods section can be expressed as

$$R_{\mathrm{N}}(\mathrm{N}_z) = (3D + C)J(\omega_{\mathrm{N}}) + DJ(|\omega_{\mathrm{H}}|+|\omega_{\mathrm{N}}|) + 6DJ(|\omega_{\mathrm{H}}|-|\omega_{\mathrm{N}}|) \quad (1)$$

$$R_{\mathrm{N}}(\mathrm{N}_x) = (2D + 2C/3)J(0) + (3D/2 + C/2)J(\omega_{\mathrm{N}}) + (D/2)J(|\omega_{\mathrm{H}}|+|\omega_{\mathrm{N}}|) + 3DJ(\omega_{\mathrm{H}}) + 3DJ(|\omega_{\mathrm{H}}|-|\omega_{\mathrm{N}}|) + R_{\mathrm{ex}} \quad (2)$$

$$R_{\mathrm{HN}}(2\mathrm{H}_z^{\mathrm{N}}\,\mathrm{N}_x) = (2D + 2C/3)J(0) + (3D/2 + C/2)J(\omega_{\mathrm{N}}) + (D/2)J(|\omega_{\mathrm{H}}|+|\omega_{\mathrm{N}}|) + 3DJ(|\omega_{\mathrm{H}}|-|\omega_{\mathrm{N}}|) + \rho_{\mathrm{H^NH^i}} + R_{\mathrm{ex}} \quad (3)$$

$$R_{\mathrm{HN}}(2\mathrm{H}_z^{\mathrm{N}}\,\mathrm{N}_z) = (3D + C)J(\omega_{\mathrm{N}}) + 3DJ(\omega_{\mathrm{H}}) + \rho_{\mathrm{H^NH^i}} \quad (4)$$

$$R_{\mathrm{H}}(\mathrm{H}_z^{\mathrm{N}}) = D[J(|\omega_{\mathrm{H}}|+|\omega_{\mathrm{N}}|) + 3J(\omega_{\mathrm{H}}) + 6J(|\omega_{\mathrm{H}}|-|\omega_{\mathrm{N}}|)] + \rho_{\mathrm{H^NH^i}} \quad (5)$$

$$R_{\mathrm{N}}(\mathrm{H}_z^{\mathrm{N}} \leftrightarrow \mathrm{N}_z) = D[6J(|\omega_{\mathrm{H}}|-|\omega_{\mathrm{N}}|) - J(|\omega_{\mathrm{H}}|+|\omega_{\mathrm{N}}|)] \quad (6)$$

The above rate constants permit the extraction of the various spectral density values. Additional relaxation rate constants for the NH spin systems include $R_{\mathrm{H}}(\mathrm{H}_x^{\mathrm{N}})$, the decay constant for in-phase amide proton transverse relaxation, $R_{\mathrm{HN}}(2\mathrm{H}_x^{\mathrm{N}}\,\mathrm{N}_z)$, the decay constant for antiphase amide proton transverse relaxation, and $R_{\mathrm{HN}}(2\mathrm{H}_x^{\mathrm{N}}\,\mathrm{N}_x)$, the decay constant for multiple quantum coherence. For completeness, these rates can be given below in terms of the spectral density values as

$$R_{\mathrm{H}}(\mathrm{H}_x^{\mathrm{N}}) = D[2J(0) + {}^1\!/_2J(|\omega_{\mathrm{H}}|+|\omega_{\mathrm{N}}|) + {}^3\!/_2J(\omega_{\mathrm{H}}) + 3J(\omega_{\mathrm{N}}) + 3J(|\omega_{\mathrm{H}}|-|\omega_{\mathrm{N}}|)] + \zeta_{\mathrm{H^NH^i}} + R_{\mathrm{ex}} \quad (6b)$$

$$R_{\mathrm{H}}(2\mathrm{H}_x^{\mathrm{N}}\,\mathrm{N}_z) = D[2J(0) + {}^1\!/_2J(|\omega_{\mathrm{H}}|+|\omega_{\mathrm{N}}|) + {}^3\!/_2J(\omega_{\mathrm{H}}) + 3J(|\omega_{\mathrm{H}}|-|\omega_{\mathrm{N}}|)] + CJ(\omega_{\mathrm{N}}) + \zeta_{\mathrm{H^NH^i}} + R_{\mathrm{ex}} \quad (6c)$$

$$R_{\mathrm{HN}}(2\mathrm{H}_x^{\mathrm{N}}\,\mathrm{N}_x) = (2C/3)J(0) + (3D/2 + C/2)J(\omega_{\mathrm{N}}) + (3D/2)J(\omega_{\mathrm{H}}) + (D/2)J(|\omega_{\mathrm{H}}|+\omega_{\mathrm{N}}|) + 3DJ(|\omega_{\mathrm{H}}|-|\omega_{\mathrm{N}}|) + \zeta_{\mathrm{H^NH^i}} + R_{\mathrm{ex}} \quad (6d)$$

Note that the $R_{\mathrm{HN}}(2\mathrm{H}_x^{\mathrm{N}}\,\mathrm{N}_x)$ constant is the average of the decay constants for the relaxation of heteronuclear double and zero quantum coherences. More detailed descriptions of the above rate constants are given elsewhere (Peng & Wagner, 1994a,b). In eqs 1−6 and 6b−d, the constant D is proportional to the mean squared value of the heteronuclear DD interaction and is given by

$$D = \frac{\hbar^2 \gamma_{\mathrm{H}}^2 \gamma_{\mathrm{N}}^2}{r_{\mathrm{NH}}^6} \quad (7)$$

In eq 7, r_{NH} is the internuclear amide ^{15}N−^{1}H bond distance, and γ_{H} and γ_{N} are the gyromagnetic ratios for the amide proton and nitrogen, respectively. $\hbar$ is Planck's constant divided by 2π. D is approximately 1.3×10^9 (rad/s)^2 for $r_{\mathrm{NH}} = 1.02$ Å (Keiter, 1986). The constant C is proportional to the mean square value of the anisotropic component of the $^{15}\mathrm{N}-B_0$ interaction and is given by

$$C = \frac{\Delta^2 \omega_{\mathrm{N}}^{\,2}}{3} \tag{8}$$

In eq 8, $\omega_{\mathrm{N}} = -\gamma_{\mathrm{N}} B_{\mathrm{o}}$, and Δ is the ^{15}N chemical shift anisotropy which is taken here to be approximately constant at −160 ppm (Hiyama et al., 1988). C is approximately 0.31, 0.87, and 1.25 (rad/s)^2 at 7.04, 11.74, and 14.1 T, respectively. Spin orders that depend explicitly upon the spin orientation of the amide proton, including $\langle 2\mathrm{H}_z^{\mathrm{N}}\,\mathrm{N}_x\rangle$, $\langle 2\mathrm{H}_z^{\mathrm{N}}\,\mathrm{N}_z\rangle$, and $\langle \mathrm{H}_z^{\mathrm{N}}\rangle$, have an additional contribution from proton−proton DD interactions as well. This contribution is denoted by $\rho_{\mathrm{H^NH^i}}$ in eqs 3−5. $\rho_{\mathrm{H^NH^i}}$ is simply the sum of proton longitudinal relaxation rate constants derived from the homonuclear DD interactions between a given amide proton $\mathrm{H^N}$ and other protons $\mathrm{H^i}$. The relative magnitudes of the constituent rate constants depend on the length of both the interproton vectors and their rapidity of reorientation. $\zeta_{\mathrm{H^NH^i}}$ in eqs 6b−d is the analogous term containing the sum of transverse relaxation rate constants derived from proton−proton DD interactions. The R_{ex} term in the $R_{\mathrm{N}}(\mathrm{N}_x)$ and $R_{\mathrm{HN}}(2\mathrm{H}_z^{\mathrm{N}}\,\mathrm{N}_x)$ expressions (eqs 2, 3, and 6b−d) reflects possible exchange effects on the transverse rate constants. $R_{\mathrm{ex}} = L\pi$, where L is the familiar exchange broadening observed in the limit of "fast chemical exchange" (i.e. only one ^{15}N resonance is seen per NH bond).

The critical pieces of dynamics information in these rate constant expressions are the five values of the spectral density function denoted by $J(0)$, $J(\omega_{\mathrm{N}})$, $J(\omega_{\mathrm{H}})$, $J(|\omega_{\mathrm{H}}|-|\omega_{\mathrm{N}}|)$, and $J(|\omega_{\mathrm{H}}|+|\omega_{\mathrm{N}}|)$. The linear relationships of eqs 1−6 can be inverted, and thus, the five spectral density values can be expressed directly in terms of the experimental relaxation rates (Peng & Wagner, 1992a,b). These formulae are given below as

$$J(0) + \lambda R_{\mathrm{ex}} = \frac{3}{4}\frac{1}{3D + C}[-{}^1\!/_2 R_{\mathrm{N}}(\mathrm{N}_z) + R_{\mathrm{N}}(\mathrm{N}_x) + R_{\mathrm{HN}}(2\mathrm{H}_z^{\mathrm{N}}\,\mathrm{N}_x) - {}^1\!/_2 R_{\mathrm{HN}}(2\mathrm{H}_z^{\mathrm{N}}\,\mathrm{N}_z) - {}^1\!/_2 R_{\mathrm{H}}(\mathrm{H}_z)] \tag{9}$$

$$J(\omega_{\mathrm{N}}) = \frac{1}{2}\frac{1}{3D + C}[R_{\mathrm{N}}(\mathrm{N}_z) + R_{\mathrm{HN}}(2\mathrm{H}_z^{\mathrm{N}}\,\mathrm{N}_z) - R_{\mathrm{H}}(\mathrm{H}_z)] \tag{10}$$

$$J(|\omega_{\mathrm{H}}|-|\omega_{\mathrm{N}}|) = \frac{1}{24D}[R_{\mathrm{N}}(\mathrm{N}_z) - R_{\mathrm{HN}}(2\mathrm{H}_z^{\mathrm{N}}\,\mathrm{N}_z) + R_{\mathrm{H}}(\mathrm{H}_z) + 2R_{\mathrm{N}}(\mathrm{H}_z^{\mathrm{N}} \leftrightarrow \mathrm{N}_z)] \tag{11}$$

$$J(\omega_{\mathrm{H}}) = \frac{1}{12D}[-R_{\mathrm{N}}(\mathrm{N}_z) + 2R_{\mathrm{N}}(\mathrm{N}_x) - 2R_{\mathrm{HN}}(2\mathrm{H}_z^{\mathrm{N}}\,\mathrm{N}_x) + R_{\mathrm{HN}}(2\mathrm{H}_z^{\mathrm{N}}\,\mathrm{N}_z) + R_{\mathrm{H}}(\mathrm{H}_z)] \tag{12}$$

$$J(|\omega_{\mathrm{H}}|+|\omega_{\mathrm{N}}|) = \frac{1}{4D}[R_{\mathrm{N}}(\mathrm{N}_z) - R_{\mathrm{HN}}(2\mathrm{H}_z^{\mathrm{N}}\,\mathrm{N}_z) + R_{\mathrm{H}}(\mathrm{H}_z) - 2R_{\mathrm{N}}(\mathrm{H}_z^{\mathrm{N}} \leftrightarrow \mathrm{N}_z)] \tag{13}$$

$$\rho_{\mathrm{H^NH^i}} = {}^1\!/_4[-R_{\mathrm{N}}(\mathrm{N}_z) - 2R_{\mathrm{N}}(\mathrm{N}_x) + 2R_{\mathrm{HN}}(2\mathrm{H}_z^{\mathrm{N}}\,\mathrm{N}_x) + R_{\mathrm{HN}}(2\mathrm{H}_z^{\mathrm{N}}\,\mathrm{N}_z) + R_{\mathrm{H}}(\mathrm{H}_z)] \tag{14}$$

At a given field strength, five values of $J(\omega)$ are obtained, as well as the contribution of the proton−proton longitudinal relaxation. Thus, for n fields, $4n + 1$ unique spectral density values are obtained. Equations 9−14 are identical to those contained in our first proposals of the spectral density-mapping approach (Peng & Wagner, 1992a,b), with the exception of the explicit inclusion of chemical exchange effects. Equation 9 shows that the zero-frequency information is the sum of both $J(0)$ and R_{ex}. λ is a scale factor $(3/2)[1/(3D + C)]$ and is approximately 0.35, 0.31, and 0.29 (ns/rad)^2 at 7.04, 11.74, and 14.1 T, respectively. In the subsequent discussion, it will be convenient to refer to an effective value of $J(0)$, denoted by $J_{\mathrm{eff}}(0)$, where

$$J_{\mathrm{eff}}(0) = J(0) + \lambda R_{\mathrm{ex}} \tag{15}$$

Note that the R_{ex} term depends on both the position of the carrier and the strength of the ^{15}N spin lock (B_1) used in the transverse relaxation experiments. Further discussion of exchange effects are given in the following sections.

It is worth emphasizing that the area under $J(\omega)$ is a constant (Abragam, 1961; Ernst et al., 1987). This constant is proportional to the mean squared energy of the orientational fluctuations driving the DD and CSA relaxation mechanisms and is the same for all NH bonds. The precise manner in which the NH bond reorients determines the shape of $J(\omega)$ and, thus, how this constant area is distributed. Fast internal motions that would tend to increase $J(\omega)$ at higher frequencies must therefore decrease intensity at lower frequencies in order to conserve the total $J(\omega)$ area. Also, larger proteins undergoing slower overall molecular tumbling are expected to have $J(\omega)$ functions more heavily weighted toward the low frequencies than those presented below for eglin c.

The spectral density functions can be modeled by analytical functions which are derived from certain *a priori* assumptions about the orientational dynamics of the NH bonds. A broad class of models is based upon the assumption that the NH bond dynamics are purely diffusive. In such models, the angular autocorrelation function $G_{\mathrm{NH}}(t)$ for a particular NH bond is expected to be sums of exponentials

$$G_{\mathrm{NH}}(t) = \sum_{\mu=0}^{\infty} A_\mu \exp(-t/\tau_\mu) \tag{16}$$

Accordingly, the spectral density function $J(\omega)$ is expected to be a sum of Lorentzians centered on $\omega = 0$, and therefore, $J(\omega)$ cannot increase with frequency (Woessner, 1962; Kinoshita et al., 1977; King & Jardetzky, 1978; Wittebort & Szabo, 1978; Richarz et al., 1980; Lipari & Szabo, 1982a,b). Currently, the most popular model form for $J(\omega)$ is based upon eq 16 and is known as the "model-free" formalism first proposed by Lipari and Szabo (1982a,b). Their approach assumes a two-term expansion of the form given in eq 16. Motions of an NH bond vector due to overall molecular tumbling and internal dynamics are assumed to be statistically independent. The internal motion amplitude is described in terms of an order parameter S^2. The internal motion autocorrelation function is approximated by a single exponential decay $S^2 + (1 - S^2)\exp(-t/\tau_{\mathrm{i}})$, which has a weight of $1 - S^2$, an effective internal motion time constant τ_{i}, and an eventual plateau value S^2. If the NH bond posseses isotropic internal motion, then $S^2 = 0$. If the NH bond lacks internal mobility, then $S^2 = 1$. If one assumes that the overall tumbling of the protein is approximately that of a sphere, and designates the overall rotational correlation time to be

τ_{rot}, then the model form for $J(\omega)$ becomes

$$J_{\mathrm{ls}}(\omega) = {}^{2}/_{5}\left[\frac{S^2\tau_{\mathrm{rot}}}{1 + (\omega\tau_{\mathrm{rot}})^2} + \frac{(1 - S^2)\tau_{\mathrm{e}}}{1 + (\omega\tau_{\mathrm{e}})^2}\right] + \delta_{\omega\mathrm{o}}\lambda R_{\mathrm{ex}} \quad (17)$$

where

$$\tau_{\mathrm{e}} = \frac{\tau_{\mathrm{i}}\tau_{\mathrm{rot}}}{\tau_{\mathrm{i}} + \tau_{\mathrm{rot}}} \quad (18)$$

and

$$\begin{aligned} \delta_{\omega\mathrm{o}} &= 1 \quad \text{if} \quad \omega = 0 \\ &= 0 \quad \text{if}\, \omega \neq 0 \end{aligned} \quad (19)$$

The additional term, $\delta_{\omega\mathrm{o}}\lambda R_{\mathrm{ex}}$, accounts for the possibility of chemical exchange effects and is not part of the original model form proposed by Lipari and Szabo (1982 a,b). λ and R_{ex} are defined as before, and the $\delta_{\omega\mathrm{o}}$ ensures that the exchange term contributes only at the zero frequency. In a protein containing n NH bonds, eq 17 calls for the optimization of potentially $3n + 1$ fitting parameters. However, one usually assumes that only a limited number of NH bonds will undergo chemical exchange processes, and therefore, the number of optimized parameters is typically much less than $3n + 1$. An extended version of eq 17 assumes a biexponential decay of the internal autocorrelation function (Clore et al., 1990a,b). The internal autocorrelation function now contains two order parameters, S_{s}^2 and S_{f}^2, and two internal motion time constants, τ_{f} and τ_{s}. The f and s subscripts signify fast and slow internal motions, respectively. In principle, the extended model presents $5n + 1$ fitting parameters. In practice, one usually assumes that $\tau_{\mathrm{f}} << \tau_{\mathrm{s}} < \tau_{\mathrm{rot}}$ and that the faster internal motions parameterized by S_{f}^2 and τ_{f} are axially symmetric (Clore et al., 1990a,b). The axial symmetry allows the factorization $S^2 = S_{\mathrm{f}}^2 S_{\mathrm{s}}^2$, and the model form of the spectral density therefore becomes

$$J_{\mathrm{ls,ext}}(\omega) = {}^{2}/_{5}S_{\mathrm{f}}^{2}\left[\frac{S_{\mathrm{s}}^2\tau_{\mathrm{rot}}}{1 + (\omega\tau_{\mathrm{rot}})^2} + \frac{(1 - S_{\mathrm{s}}^2)\tau_{\mathrm{se}}}{1 + (\omega\tau_{\mathrm{se}})^2}\right] + \delta_{\omega\mathrm{o}}\lambda R_{\mathrm{ex}} \quad (20)$$

where $\tau_{\mathrm{se}} = \tau_{\mathrm{s}}\tau_{\mathrm{rot}}/(\tau_{\mathrm{s}} + \tau_{\mathrm{rot}})$. In the limit that $S_{\mathrm{f}}^2 = 1.0$, S_{s}^2 and τ_{s} reduce to S^2 and τ_{e}, respectively, as given in the simpler $J_{\mathrm{ls}}(\omega)$.

Behavior of the Relaxation Rates. Significant reductions in the relaxation rate constants are seen for NH bonds within the first eight N-terminal residues and the protease binding loop residues (residues 43–47). The first eight N-terminal residues have the smallest relaxation rates. The rates increase in a nearly monotonic fashion until values typical of the protein core occur at Ser9. The binding loop residues have rates intermediate between those of the core residues and the first eight N-terminal residues. Thus, in the case of eglin c, the relaxation rates can distinguish those NH bonds involved in secondary structure from those that are not. However, they apparently do not distinguish between the different kinds of secondary structure present. Figure 1A–F contains plots of the relaxation rate constants for several residues from representative regions of eglin c. The rates are plotted as a function of B_0. The average values of the rate constants and the average uncertainties are given in Table 1. The averages do not include those NH bonds belonging to the first eight N-terminal residues or those in the binding loop segment. Tables listing all rate constants at all fields are provided in the supporting information. NH bonds for which resonance overlap compromised the accuracy of the fitted rate constants are indicated in the supporting information tables.

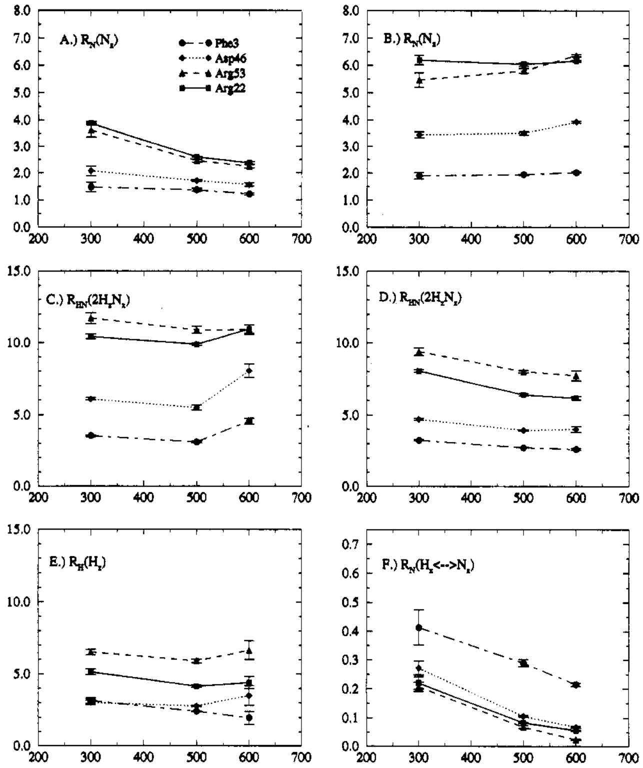

FIGURE 1: Relaxation rate constants as a function of spectrometer field strength, for four representative NH bonds in eglin c. The data were recorded at 7.04, 11.74, and 14.1 T. Field strengths are delineated in terms of the corresponding ^{1}H resonance frequency: (A) $R_{\mathrm{N}}(\mathrm{N}_z)$, (B) $R_{\mathrm{N}}(\mathrm{N}_x)$, (C) $R_{\mathrm{HN}}(2\mathrm{H}_z^{\mathrm{N}}\,\mathrm{N}_x)$, (D) $R_{\mathrm{HN}}(2\mathrm{H}_z^{\mathrm{N}}\,\mathrm{N}_z)$, (E) $\mathrm{R}_{\mathrm{H}}(\mathrm{H}_z)$, (F) $R_{\mathrm{N}}(\mathrm{H}_z \leftrightarrow \mathrm{N}_z)$. The residues include Phe3 (N-terminus), Arg22 (α-helix), Arg53 (β-strand), and Asp46 (protease binding loop). Solid lines with squares indicate Arg22, dashed lines with triangles denote Arg53, dotted lines with diamonds indicate Asp46, and dotted-dashed lines with circles denote Phe3. Systematic decreases of the rate constants with B_{o} are observed for $R_{\mathrm{N}}(\mathrm{N}_z)$, $R_{\mathrm{HN}}(2\mathrm{H}_z^{\mathrm{N}}\,\mathrm{N}_z)$, and $R_{\mathrm{N}}(\mathrm{H}_z \leftrightarrow \mathrm{N}_z)$.

Table 1: Average Relaxation Rate Constants (s^{-1}) for Eglin C at 7.04, 11.74, and 14.1 T[a]

parameter[b,c]	7.04 T	11.74 T	14.1 T
$R_{\mathrm{N}}(\mathrm{N}_z)$	3.58 ± 0.05	2.48 ± 0.05	2.26 ± 0.05
$R_{\mathrm{N}}(\mathrm{N}_x)$	5.66 ± 0.22	5.61 ± 0.08	6.10 ± 0.20
$R_{\mathrm{HN}}(2\mathrm{H}_z^{\mathrm{N}}\,\mathrm{N}_x)$	10.06 ± 0.16	9.59 ± 0.42	10.89 ± 0.27
$R_{\mathrm{HN}}(2\mathrm{H}_z^{\mathrm{N}}\,\mathrm{N}_z)$	7.88 ± 0.14	6.45 ± 0.15	6.37 ± 0.26
$R_{\mathrm{H}}(\mathrm{H}_z^{\mathrm{N}})$	5.15 ± 0.22	4.62 ± 0.27	5.06 ± 0.60
$R_{\mathrm{N}}(\mathrm{H}_z^{\mathrm{N}} \leftrightarrow \mathrm{N}_z)$	0.22 ± 0.02	0.08 ± 0.01	0.04 ± 0.01
NOE	-0.60 ± 0.07	-0.32 ± 0.02	-0.19 ± 0.013

[a] pH = 3.0, temperature = 36 °C, 3.8 mM. [b] Rates and uncertainties are averaged over NH bonds that do not show evidence of fast internal motion and include 51 residues. [c] NOE values are dimensionless.

At all magnetic field strengths, the two-spin NH relaxation rates $R_{\mathrm{HN}}(2\mathrm{H}_z^{\mathrm{N}}\,\mathrm{N}_x)$ and $R_{\mathrm{HN}}(2\mathrm{H}_z^{\mathrm{N}}\,\mathrm{N}_z)$ and the amide proton longitudinal relaxation rate $R_{\mathrm{H}}(\mathrm{H}_z^{\mathrm{N}})$ show significantly more variability with sequence than their one-spin counterparts [i.e. $R_{\mathrm{N}}(\mathrm{N}_z)$, $R_{\mathrm{N}}(\mathrm{N}_x)$, and $R_{\mathrm{N}}(\mathrm{H}_z^{\mathrm{N}} \leftrightarrow \mathrm{N}_z)$]. Since the pattern of sequence variability is well-reproduced at all three B_o values, what is most likely being observed are the contributions of different proton–proton DD relaxation pathways contained in the $\rho_{H^NH^i}$ terms (cf. eqs 4 and 5), which depend heavily on the specific interproton distances. It is worth noting that $R_N(N_z)$ displays more variability with protein sequence at lower field strengths. An example is the rise and fall of $R_N(N_z)$ from Thr17 to Thr26, with a maximum value at Arg22. This feature is quite clear at 7.04 T and successively less distinct as one moves to a higher B_o. This suggests that $R_N(N_z)$ at 7.04 T explores a frequency range in which the individual backbone NH $J(\omega)$ functions show more variability among themselves.

The variation of the relaxation rates with the B_o strength stems from several origins. The first is the expected effect, that different B_o values cause the relaxation rates to sample the $J(\omega)$ functions at different frequencies. The size of this B_o sensitivity depends both on the shape of $J(\omega)$ and on the specific linear combination of $J(\omega)$ values defining the rate constant. A second cause stems from the ^{15}N CSA-induced relaxation. The factor C given in eq 8 introduces an explicit quadratic dependence on B_o, thereby enhancing the CSA-induced relaxation at higher field strengths. A third cause of B_o dependence pertains only to the transverse relaxation rates, $R_N(N_x)$ and $R_{HN}(2H_z^N N_x)$. As stated, these rates may be enhanced by chemical exchange processes. Higher field strengths effectively increase the resonance frequency differences germane to the potential exchange processes. As a result, the R_{ex} contributions of eqs 2 and 3 also scale quadratically with ω_N, provided the potential exchange processes remain in the fast exchange regime. This is the case for the NH resonances analyzed here, as only a single set of NH correlations are observed at all field strengths. Of course, the situation becomes more complex if the exchange processes enter the intermediate exchange regime. However, in such cases, the NH resonances typically disappear, thereby precluding further analysis.

The experimental results demonstrate that the longitudinal relaxation rate constant, $R_N(N_z)$, the longitudinal two-spin order relaxation rate constant, $R_{HN}(2H_z^N N_z)$, and the heteronuclear cross-relaxation rate, $R_N(H_z^N \leftrightarrow N_z)$, display the strongest variation with B_o. Specifically, these rates show a clear, systematic decrease with increasing B_o. These decreases can be understood from eqs 1, 4, and 6. Note that eq 1 shows that the leading term of $R_N(N_z)$ depends on B_o via both the $J(\omega_N)$ sampling and the CSA factor C. The observed decrease of $R_N(N_z)$ with increasing B_o indicates that the magnitude of $J(\omega_N)$ decreases faster than the CSA contribution C increases. The decrease of $R_{HN}(2H_z^N N_z)$ with B_o, while quite clear, is less pronounced than in the case of $R_N(N_z)$. The decrease is partially obfuscated by the large contribution of the amide proton spin lattice relaxation, $\rho_{H^NH^i}$. While this latter proton longitudinal relaxation may also be affected by proton CSA (Dalvit & Bodenhausen, 1989; Dalvit, 1991), the effect is expected to be rather weak. For example, recent solid-state NMR studies have revealed an amide proton CSA of approximately 13 ppm (Gerald et al., 1993). Additionally, the proton–proton DD terms in $\rho_{H^NH^i}$ depend on different spectral density functions that are dominated by zero-frequency contributions. As a result, the DD terms of $\rho_{H^NH^i}$ are also not expected to depend significantly on the external field. The decrease of $R_N(H_z^N \leftrightarrow N_z)$ with B_o is manifested by the shrinking magnitude of the steady-state heteronuclear NOE with increasing field. Since NOE $= (\gamma_H/\gamma_N)[R_N(H_z^N \leftrightarrow N_z)/R_N(N_z)]$ and $R_N(N_z)$ is observed to decrease with B_o, a decrease in the absolute value of the NOE demands that $R_N(H_z^N \leftrightarrow N_z)$ decrease more steeply than $R_N(N_z)$. As eq 6 shows, this cross-relaxation rate constant is CSA independent. The observed reduction of this rate constant exclusively reflects the effect of different B_o strengths sampling $J(\omega)$ at different frequencies.

The in-phase and antiphase transverse relaxation rate constants, $R_N(N_x)$ and $R_{HN}(2H_z^N N_x)$, show much less systematic variation with B_o. As seen from eqs 2 and 3, the transverse rates are dominated by spectral density samplings near the zero frequency. Slight increases at higher field would be expected from the aforementioned quadratic B_o dependence contained within the CSA factor C multiplying the $J(0)$ term. Such expectations are borne out by the experiments in that the in-phase transverse relaxation rates are slightly larger, on average, at 14.1 T. The amide proton longitudinal rates are expected also to be nearly independent of B_o. Their leading term is essentially a net zero-frequency contribution in the $\rho_{H^NH^i}$ term, and there is no ^{15}N CSA factor involved. This lack of variation is essentially what is seen in the data.

The observed B_o dependence of the NH relaxation rate constants can be compared with that predicted by model forms of $J(\omega)$. Figure 2A,B profiles the six measured relaxation parameters for a range of B_o values spanning proton resonance frequencies from 100 to 1000 MHz. CSA values of -160 ppm (Hiyama et al., 1989) and -9 ppm (Dalvit & Bodenhausen, 1989) were assumed for the ^{15}N and ^{1}H nuclei, respectively. The model form for $J(\omega)$ is the two-Lorenztian expression of Lipari and Szabo (1982a,b) given in eq 17. Figure 2A depicts the expected rates for an isotropically tumbling protein having an overall rotational correlation time of $\tau_{rot} = 4.0$ ns/rad, while Figure 2B illustrates the case for $\tau_{rot} = 10.0$ ns/rad. Both figures have $S^2 = 0.8$ and $\tau_i = 20$ ps/rad. Additionally, $R_{ex} = 0$ for both figures, and so the effects of exchange are not included. The contribution of proton–proton DD longitudinal relaxation is included by setting $\rho_{H^NH^i} = 4.0\ s^{-1}$. This value is typical for the NH bonds belonging to the stuctured core of eglin c. In Figure 2B, $\rho_{H^NH^i}$ is set to 10.0 s^{-1} to account for the increase in τ_{rot} from 4.0 to 10.0 ns/rad. Note that the S^2 and τ_i parameters are typical of protein NH bonds in regions of well-defined structure. The τ_{rot} values of 4.0 and 10.0 ns/rad are intended to correspond to τ_{rot} values characteristic of small and intermediate-sized proteins, respectively. Figure 2A,B shows that $J_{ls}(\omega)$ (eq 17) predicts essentially the same dispersion behavior for the relaxation rates as the experimental data. Also depicted are $R_H(H_x^N)$ and $R_{HN}(2H_x^N N_x)$. $R_H(H_x^N)$ is the rate constant for the decay of amide proton in-phase single quantum coherence, and $R_{HN}(2H_x^N N_x)$ is the rate constant for the decay of multiple quantum coherence. Rigorously, $R_{HN}(2H_x^N N_x)$ is the average of both heteronuclear double quantum and zero quantum relaxation rate constants. However, we consider it here, since $2H_x^N N_x$ is the spin order used in heteronuclear multiple quantum experiments. Proton–proton DD transverse relaxation rate constants, $\zeta_{H^NH^i}$, contribute significantly to both $R_H(H_x^N)$ and $R_{HN}(2H_x^N N_x)$. Here, values of 10.0 and 25.0 s^{-1} were used in Figure 2A,B, respectively, to approximate the transverse

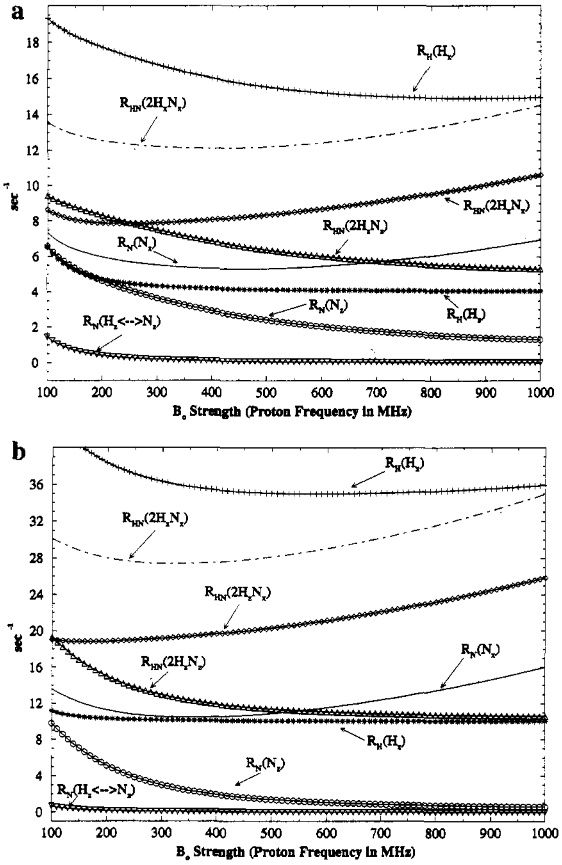

FIGURE 2: Simulations of NH relaxation rate constants as a function of the spectrometer field strength, B_o. An NH bond of length 1.02 Å was assumed, and the spectral density function given in eq 17 was used to calculate the rate constants. Two simulations are depicted, and both assume $R_{ex} = 0$, $S^2 = 0.8$, and $\tau_i = 20$ ps/rad. The two simulations differ in the value for the overall molecular rotational correlation time, τ_{rot}. (A) $\tau_{rot} = 4.0$ ns/rad and (B) $\tau_{rot} = 10.0$ ns/rad. The two different simulations are intended to correspond to an NH bond embedded in a small- (A) and intermediate-sized (B) protein molecule.

proton−proton $\zeta_{H^NH^i}$ contributions. These values assume that the ratio $\zeta_{H^NH^i}/\rho_{H^NH^i}$ approaches ≈2.5 in the spin-diffusion limit (i.e. large τ_{rot}), which is apparent if one considers only the zero-frequency spectral density contributions of the proton DD relaxation. It is worth noting that $R_{HN}(2H_x^N N_x)$ remains larger than $R_{HN}(2H_z^N N_x)$ for all values of B_o displayed. This inequality of course depends on our estimates for $\rho_{H^NH^i}$ and $\zeta_{H^NH^i}$. It further suggests that, from relaxation considerations, heteronuclear correlation experiments using the multiple quantum coherence $2H_x^N N_x$ instead of the single quantum coherence $2H_z^N N_x$ for ^{15}N shift evolution would be less sensitive.

Spectral Density Values versus Protein Sequence. The formulae in eqs 11−16 convert the NH relaxation rate constants at a given field strength B_o into five spectral density values, including $J_{eff}(0)$, $J(\omega_N)$, $J(\omega_H)$, $J(|\omega_H|-|\omega_N|)$, and $J(|\omega_H|+|\omega_N|)$. Together, the three B_o fields evaluate the $J(\omega)$ of each NH bond at approximately 0, 30, 50, 60, 270, 300, 330, 450, 500, 540, 550, 600, and 660 MHz. These values are listed in the supporting information.

Figure 3 shows the behavior of the $J(\omega)$ values with protein sequence. From here on, we refer to the $J_{eff}(0)$, J(30 MHz), J(50 MHz), and J(60 MHz) values as the low-frequency values of $J(\omega)$; these correspond to the $J(0)$ and $J(\omega_N)$ seen in eqs 9 and 10. The remaining values of $J(\omega_H)$, $J(|\omega_H|-|\omega_N|)$, and $J(|\omega_H|+|\omega_N|)$ are designated high-frequency samplings of $J(\omega)$; these values effectively characterize $J(\omega)$ in a neighborhood of $\pm\omega_N$ about ω_H. For these high-frequency values, Figure 3 plots $J_{avg}(\omega_H)$, which is obtained by averaging the high-frequency $J(\omega)$ values at a given B_o through the relation $J_{avg}(\omega_H) = {}^1/_3[J(\omega_H) + J(|\omega_H|-|\omega_N|) + J(|\omega_H|+|\omega_N|)]$. Similarly, Figure 3 plots the field-averaged value of $J_{eff}(0)$ which is simply $J_{eff}^{avg}(0) = {}^1/_3[J_{7.04T,eff}(0) + J_{11.74T,eff}(0) + J_{14.1T,eff}(0)]$.

The most notable feature of Figure 3 is the substantial reduction of $J(\omega)$ in two regions of the protein backbone. These regions include the first eight N-terminal residues (Thr1−Lys8) and an internal segment of residues (Val43−Leu47). The first seven residues do not appear in the crystal structures of eglin c in complex with subtilisin Carlsberg (McPhalen et al., 1985; McPhalen & James, 1987, 1988). In the crystal structure of free eglin c (Hipler et al., 1992), the N-terminal segment can be located, although with some degree of uncertainty, as it occupies the only large solvent cavity in the crystal. There is one intermolecular salt bridge between the side chains of Glu2 and Arg53, indicating that the defined state of the N-terminus in this crystal structure is a consequence of crystal contacts. The internal segment corresponds to the active site binding loop of eglin c and harbors the scissile bond between Leu45 and Asp46 that would normally be cleaved in the peptide substrate (McPhalen et al., 1987; Heinz et al., 1992). These reductions were first seen in the original 11.74 T data (Peng & Wagner, 1992b) and are reproduced at 7.04 and 14.1 T. The relative variation of $J(\omega)$ is much less significant for the remainder of the protein backbone, which includes regions of α-helix, β-strand, and tight turns (Hyberts & Wagner, 1990; Hyberts et al., 1992). As foreshadowed by the relaxation rate constants themselves, the different elements of well-defined secondary structure in eglin c do not distinguish themselves in the NH spectral density functions. This lack of a significant correlation between secondary structure and $J(\omega)$ also corroborates similar observations made at 11.74 T (Peng & Wagner, 1992b).

As indicated in the section about theoretical background, the reduction of the spectral density values in the N-terminal and binding loop NH bonds is indicative of enhanced internal mobility. The presence of additional rapid internal motions occurring on time scales comparable to or less than overall molecular tumbling causes these NH bonds to reorient more rapidly than the other NH bonds. As a result, the angular correlation functions of these bonds decay faster, and hence, $J(\omega)$ functions of these bonds broaden out. This broadening decreases the magnitude of $J(\omega)$ at the low frequencies in order to conserve the area under $J(\omega)$.

Figure 3 also points to a progressive loss of sequence variability in the spectral density values as one moves to higher frequencies. In particular, the $J_{eff}(0)$ profile reveals the largest variability with protein sequence. The J(30 MHz), J(50 MHz), and J(60 MHz) plots show that the $J_{eff}(0)$ profile is echoed at the $J(\omega_N)$ values, albeit with progressively less distinction. Finally, J_{avg}(300 MHz), J_{avg}(500 MHz), and J_{avg}(600 MHz) appear essentially uniform along the protein backbone. This lack of variation in the high-frequency spectral density values is due partly to the extreme sensitivity of the high-frequency $J(\omega)$ values to statistical and systematic errors in the measured relaxation rate constants. The use of

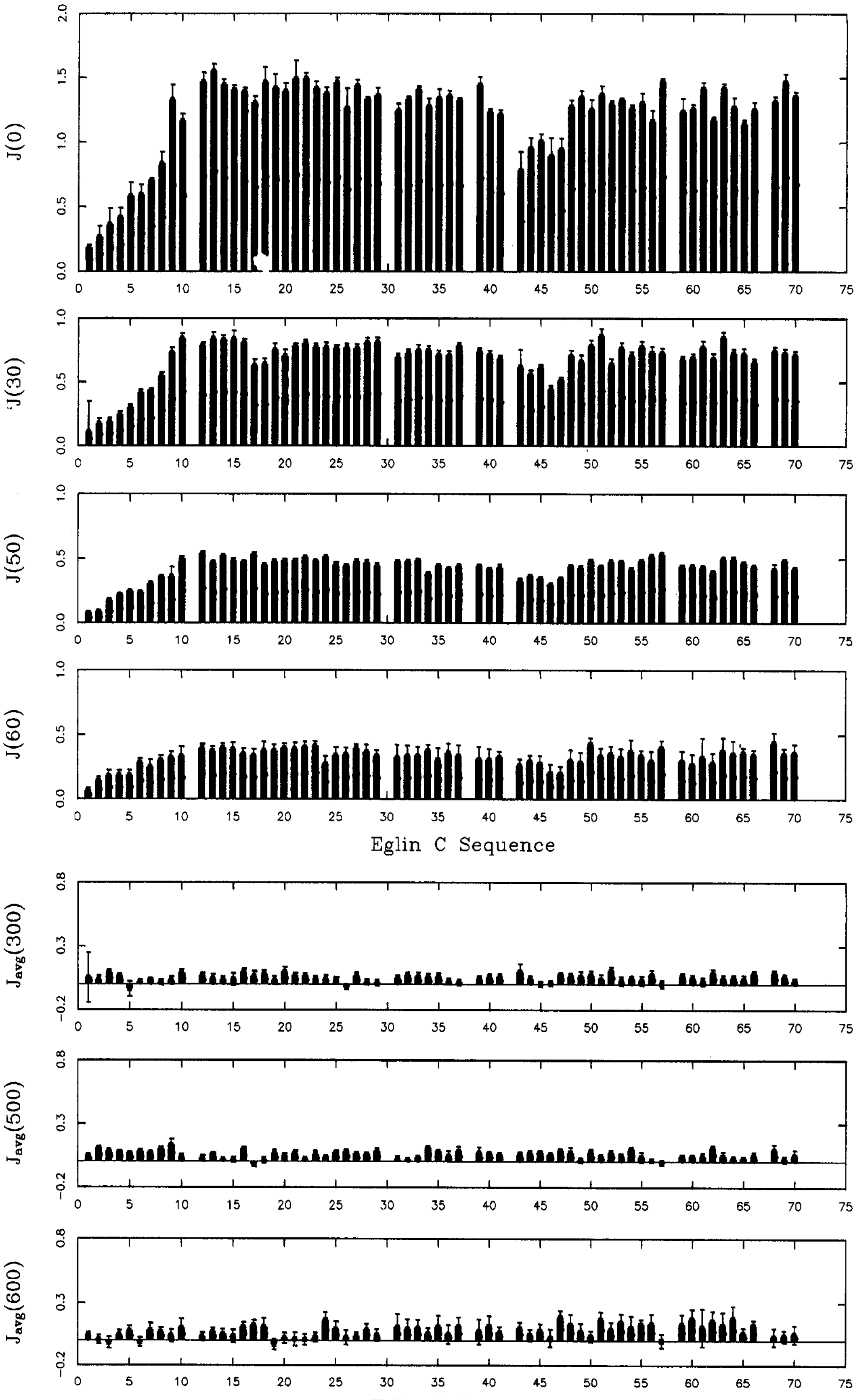

FIGURE 3: Bar graphs of the spectral density values versus protein sequence using eqs 9–13 in the text. Only the average values $J_{avg}(\omega_H) = {}^1/_3[\ J(|\omega_H|-|\omega_N|) + J(\omega_H) + J(|\omega_H|-|\omega_N|)]$ are plotted for each field strength. $J(0)$ is also averaged over the three field strengths. Attenuated $J(\omega)$ values are observed for the N-terminal residues, and the binding loop residues are Val43–Leu47. These attenuations are indicative of enhanced internal mobility.

a reduced spectral density-mapping approach (Wagner, 1994; Farrow et al., 1995; Lefévre et al., 1996) dramatically attenuates the sensitivity of the high-frequency $J(\omega)$ values to the statistical errors and, in doing so, reveals some systematic variability of the high-frequency spectral density values. This is discussed in more detail in the following sections. However, it is clear that dynamic heterogeneity along the eglin c backbone is manifested much more clearly in the frequency range below 300 MHz. The relative uniformity of the higher frequency $J(\omega)$ functions suggests that motions in this frequency range represent fast local fluctuations common to all NH bond vectors.

As stated, $J_{\text{eff}}(0)$ is apparently the most sensitive probe for dynamic heterogeneity along the protein backbone. Inspection of $J_{\text{eff}}(0)$ versus sequence alone supplies a rapid overview of the relative mobility along the protein backbone. In particular, knowledge of $J_{\text{eff}}(0)$ versus protein sequence can identify both fast and slow dynamic processes in the protein. Anomalously low $J_{\text{eff}}(0)$ values indicate the presence of fast internal motions operating on a nanosecond to subnanosecond time scale. Anomalously high $J_{\text{eff}}(0)$ values suggest the presence of significant R_{ex} contributions, as seen in eq 9. The exchange processes pertaining to the R_{ex} contributions typically operate on the millisecond to microsecond time scale and thus occur on time scales much slower than molecular reorientation. As seen in Figure 3, the collection of $J_{\text{eff}}(0)$ values does exhibit some dramatic decreases; however, they do not contain any spuriously large increases. This could be anticipated by the lack of any anomalously large $R_{\text{N}}(\text{N}_x)$ and $R_{\text{HN}}(2\text{H}_z^{\text{N}}\,\text{N}_x)$ in the experimental data. Anomalously large transverse relaxation rates are indicative of internal motions dominated by exchange processes. Thus, for the NH bonds of eglin c, internal motions dominated by exchange processes alone are not evident.

Figure 4A–D show individual $J(\omega)$ versus frequency profiles for four residues of eglin c. These residues come from different structural building blocks of eglin c and include Phe3 (N-terminus), Arg22 (α-helix), Asp46 (protease binding loop), and Arg53 (parallel β-sheet). As such, they provide illustrations of the typical shapes of $J(\omega)$ observed in eglin c. For all residues, $J_{\text{eff}}(0)$ is the maximal value. The values averaged from the three fields are 0.36 ± 0.12, 1.49 ± 0.05, 0.90 ± 0.14, and 1.32 ± 0.01 ns/rad for Phe3, Arg22, Asp46, and Arg53, respectively. A comparison of the $J(\omega)$ profiles from Phe3 and Arg22 provides the clearest illustration of the effects of increased internal motion. Most noticeably, the average $J_{\text{eff}}(0)$ value of Phe3 (0.36 ± 0.12 ns/rad) is less than a third of that belonging to Arg22 (1.49 ± 0.05 ns/rad). Additionally, the shape of the Phe3 spectral density is relatively flat when compared to that of Arg22. The low $J_{\text{eff}}(0)$ and flatter frequency distribution for Phe3 is consistent with the aforementioned theoretical expectations. Arg53 shows a distribution similar to that of Arg22. While the average $J_{\text{eff}}(0)$ value of Asp46 (0.90 ± 0.14 ns/rad) is significantly reduced from that of Arg22, the whole $J(\omega)$ shape does not appear as flat as that of Phe3; rather, it appears as a scaled down version of those of Arg22 and Arg53. Thus, the mobility of Asp46 is intermediate between that of Phe3 and Arg22. In some cases, the values of $J_{\text{eff}}(0)$ obtained from the different field strengths vary significantly. This variability may be due to the presence of chemical exchange processes, and this is discussed in more detail below.

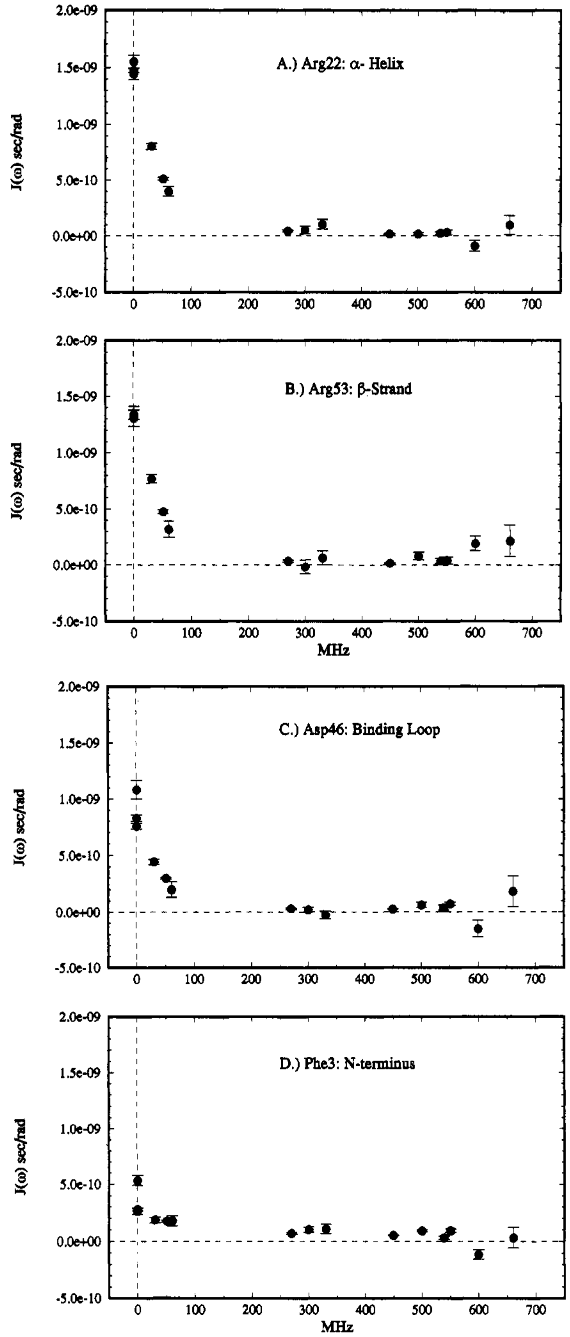

FIGURE 4: Spectral density profiles resulting from the relaxation measurements at 7.04, 11.74, and 14.1 T for the amide NH bonds of (A) Arg22, (B) Arg53, (C) Asp46, and (D) Phe3. Equations 9–13 in the text were used to extract 15 spectral density values (13 unique) for each NH bond.

The six relaxation parameters in eqs 1–6 have also been measured for the side chain ϵ-NH bonds of Arg22, -48, -51, and -53. Such measurements have been performed only at 11.74 T; thus, the spectral density functions of these side chain NH bonds are not characterized as completely as those of the backbone NH bonds. Nonetheless, a comparison of the ϵ and backbone $J(\omega)$ values at 11.74 T does provide some information on side chain mobilities. In particular, the $J_{\text{eff}}(0)$ and $J(50\text{ MHz})$ values of the Arg51 ϵ-NH bond are ≈80 and 86% of that of the backbone NH values, respectively. The similarity of $J(\omega)$ values at the amide and ϵ-positions therefore suggests restricted side chain mobility for Arg51. Independent corroborating evidence for this restriction is the unusually large downfield shift of the ϵ-proton (9.12 ppm). The downfield shift indicates involvement in a strong hydrogen bond, which could conceivably hinder the orientational freedom of the ϵ-NH bond. In contrast, the $J_{\text{eff}}(0)$ values for the ϵ-NH bonds of Arg22 and Arg48 are only ≈30% of the corresponding amide backbone values and have magnitudes typical of the flexible N-terminal residues. These $J_{\rm eff}(0)$ reductions suggest considerable side chain mobility for Arg22 and Arg48. The $J_{\rm eff}(0)$ value of Arg53 ϵ-NH is $\approx$65% of the corresponding backbone value and has a value similar to those of the backbone NH bonds in the protease binding loop. Thus, while the Arg53 side chain enjoys more mobility than the side chain Arg51, it clearly does not possess the same motional freedom seen for the Arg22 and Arg48 side chains. In the crystal structure of complexed eglin c, the side chains of Arg51 and Arg53 are involved in hydrogen bond contacts with the binding loop residues Asp46 and Thr44, respectively (Heinz et al., 1991). Such hydrogen bonds could conceivably restrict the motional freedom of the Arg51 and Arg53 side chains. It should be noted that these particular hydrogen bonds are lost in the crystal structure of free eglin c (Hipler et al., 1992). However, this loss appears to be a consequence of crystal contacts; therefore, the hydrogen bonds seen in the complexed crystal structure may still exist for free eglin c in the solution state.

Reduced Spectral Density Functions. In the previous study at 11.74 T, anomalous behavior at the high frequency $J(\omega)$ values was seen (Peng & Wagner, 1992b). The behavior consisted of occasional negative values for $J(\omega)$ and an apparent slight increase of $J(\omega)$ at high frequencies for many residues. From physical considerations, negative values for $J(\omega)$ are impossible, as the power spectral density is essentially a probability distribution and, therefore, a positive definite function (Abragam, 1961). Increases of the spectral density at higher frequency are also forbidden, if one assumes that the NH bonds undergo purely diffusive motion. Note that increases in $J(\omega)$ would be conceivable if the NH autocorrelation functions possessed an oscillatory character. However, in the purely diffusive case, the NH autocorrelation functions would be sums of exponentials, and therefore, each $J(\omega)$ would be a sum of Lorenztians centered at $\omega = 0$. The newer relaxation data at 7.04 and 14.1 T also show the dual anomalies of negative $J(\omega)$ values and increasing $J(\omega)$ values. Given this, we believe that the high-frequency anomalies mainly reflect the high sensitivity of the $J(\omega_H)$ and $J(|\omega_H|\pm|\omega_N|)$ values to statistical fluctuations and potential systematic errors in the relaxation rate constants.

The high sensitivity of $J(\omega_H)$ and $J(|\omega_H|\pm|\omega_N|)$ to random errors can be understood from eqs 11–13. These expressions calculate potentially very small quantities by taking differences of large numbers. Random errors in these rate constants can lead to errors that are of a magnitude similar to that of the target spectral density values themselves, and thus, the $J(\omega)$ values can be overestimated or underestimated by over 100%. If the spectral density functions are monotonically decreasing functions of frequency, then these difficulties will only increase at higher B_o. This can be illustrated by estimation of the required experimental precision in order to ensure that $J(|\omega_H|+|\omega_N|)$ and $J(|\omega_H|-|\omega_N|)$ remain positive and that $J(|\omega_H|-|\omega_N|)$ is greater than $J(|\omega_H|+|\omega_N|)$. Using eqs 11 and 13, we can describe this precision in terms of a double inequality involving the heteronuclear cross-relaxation rate constant. This inequality is given as

$$^{14}/_5 R_N(H_z^N \leftrightarrow N_z) > R_N(N_z) + R_H(H_z) - R_{HN}(2H_z^N N_z) > 2R_N(H_z^N \leftrightarrow N_z)$$

Thus, one must be able to define the middle sum and difference with a precision on the order of $^4/_5 R_N(H_z^N \leftrightarrow N_z)$. However, as seen experimentally, this cross-relaxation rate constant becomes increasingly smaller at higher B_o. At 14.1 T, the required precision is thus $\approx 0.05\ {\rm s}^{-1}$. Given that the estimated errors for $R_H(H_z^N)$ alone are typically on the order of $0.21\ {\rm s}^{-1}$, such precision is beyond the reach of actual experiments. The situation is somewhat improved at 11.74 T, in which the required precision is $\approx 0.08\ {\rm s}^{-1}$. However, it is only at 7.04 T that the precision requirements become more realistic at $\approx 0.19\ {\rm s}^{-1}$. In fact, experimentally, the high-frequency anomalies are most significant at 14.1 T and least significant at 7.04 T. Note that, if the NH bond motions are diffusive, then relaxation properties of a large protein at moderate field would be expected to be similar to those of a smaller protein at higher field. One would therefore expect the high-frequency spectral density anomalies to surface more violently at lower B_o fields for proteins larger than eglin c.

Systematic errors in the measured relaxation rates also render accurate and precise determinations of $J(\omega_H)$ and $J(|\omega_H|\pm|\omega_N|)$ difficult. As stated previously (Peng & Wagner, 1992b), the experiments to measure $R_{HN}(2H_z^N N_z)$, $R_{HN}(2H_z^N N_x)$, and $R_H(H_z^N)$ are not completely satisfactory with respect to eliminating cross-relaxation pathways induced by either proton–proton DD interactions or ^{15}N DD CSA cross-correlations. Such processes render the relaxation kinetics multiexponential, and therefore, fits to single exponential functions will introduce systematic errors. To improve suppression of these cross-relaxation pathways, we have investigated the use of periodic rf schemes applied during the parametric relaxation delay, which result in a time averaging of relaxation rate constants. Such rf schemes have been developed by Fejzo et al. (1991) and exploit the opposite signs of the proton–proton NOE and ROE cross-relaxation rate constants in the limit of slow molecular tumbling. Expressions to extract spectral density values from the modified NH relaxation rate constants similar to eqs 9–13 have also been derived. The success of these sequences in quenching unwanted cross-relaxation is still under investigation. Alternatively, one could also consider modifying the protein instead of the pulse sequences. Use of deuterated protein would greatly reduce the problems of proton–proton DD cross-relaxation, as only the amide–amide cross-relaxation would have to be considered.

In this study, we have chosen to circumvent the above difficulties by replacing $J(\omega_H)$ and $J(|\omega_H|\pm|\omega_N|)$ with a single high-frequency value, $J_{\rm red}^{\rm hifreq}$, where the subscript "red" denotes reduced. This approach has already been described by several groups (Wagner, 1994; Farrow et al., 1995; Lefévre et al., 1996). $J_{\rm red}^{\rm hifreq}$ is derived from the approximation that $J(\omega)$ is essentially flat at ω_H and $|\omega_H| \pm |\omega_N|$. Therefore,

$$J_{\rm red}^{\rm hifreq} = J(|\omega_H|+|\omega_N|) = J(|\omega_H|-|\omega_N|) = J(|\omega_H|) \quad (21)$$

Such an assumption is reasonable in the case of eglin c, given that the heteronuclear cross-relaxation rate constants, $R_N(H_z^N \leftrightarrow N_z)$, become increasingly smaller at high B_o. Use of $J_{\rm red}^{\rm hifreq}$ reduces the number of spectral density values to be solved for (at fixed B_o) to three. While one could choose any subset of rate constants from the original six, the single spin order rate constants, $R_N(N_z)$ and $R_N(N_x)$, and the cross-relaxation rate $R_N(H_z^N \leftrightarrow N_z)$ are obviously preferable since

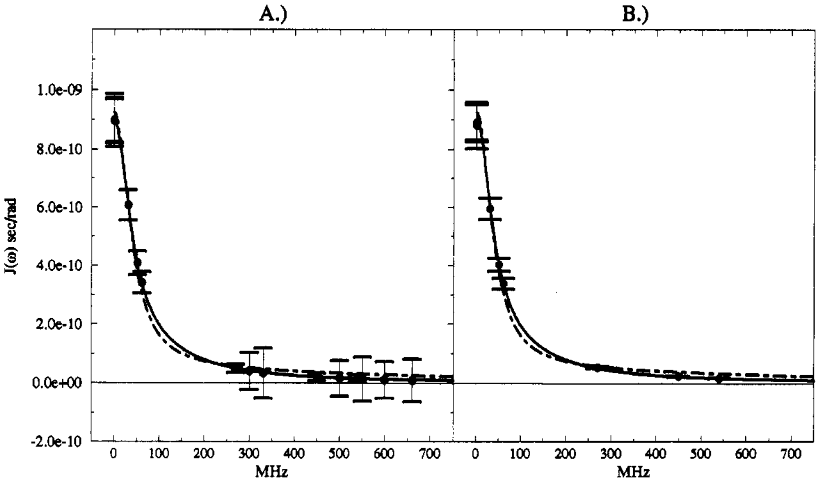

FIGURE 5: Comparison of the error-propagation properties of the (A) full spectral density-mapping approach (eqs 9–13 in the text) and the (B) reduced approach (eqs 22–24 in the text). The model form of $J_{\mathrm{ls,ext}}(\omega)$ given in eq 20 was assumed with $S_s^2 = 0.68$, $S_f^2 = 0.8$, $\tau_{\mathrm{rot}} = 8.0$ ns/rad, and $\tau_s = 1$ ns/rad. Rate constants were calculated from $J_{\mathrm{ls,ext}}(\omega)$, and 5% fractional uncertainties were assumed of the rates. The solid curves represent the model forms, and the dots and error bars indicate the back-calculated spectral densities with their associated errors. The errors for the high-frequency $J(\omega)$ values exceed 200% in the full-mapping case. The dashed line is a fit of back-calculated spectral densities to the simpler $J_{\mathrm{ls}}(\omega)$ of eq 17. The improved precision of the reduced spectral density mapping procedure can distinguish between $J_{\mathrm{ls,ext}}$ and J_{ls}.

these avoid the aforementioned complications of proton–proton DD relaxation. The spectral density formulae then simplify to

$$J_{\mathrm{red,eff}}(0) = J_{\mathrm{red}}(0) + \lambda R_{\mathrm{ex}} = \frac{3}{2}\frac{1}{3D + C}[-{}^{1}\!/_{2}R_{\mathrm{N}}(\mathrm{N}_z) + R_{\mathrm{N}}(\mathrm{N}_x) - {}^{3}\!/_{5}R_{\mathrm{N}}(\mathrm{H}_z^{\mathrm{N}} \leftrightarrow \mathrm{N}_z)] \tag{22}$$

$$J_{\mathrm{red}}(\omega_{\mathrm{N}}) = \frac{1}{3D + C}[R_{\mathrm{N}}(\mathrm{N}_z) - {}^{7}\!/_{5}R_{\mathrm{N}}(\mathrm{H}_z^{\mathrm{N}} \leftrightarrow \mathrm{N}_z)] \tag{23}$$

$$J_{\mathrm{red}}^{\mathrm{hifreq}} = \frac{1}{5D}R_{\mathrm{N}}(\mathrm{H}_z^{\mathrm{N}} \leftrightarrow \mathrm{N}_z) \tag{24}$$

The deviations between $J_{\mathrm{red}}(\omega)$ and $J(\omega)$ can be clarified by expressing the rate constants in eqs 22–24 in terms of the true $J(\omega)$ values given in eqs 1–6. The results are

$$J_{\mathrm{red,eff}}(0) = J_{\mathrm{eff}}(0)\left[1 - \frac{9}{10}\frac{1}{3 + C/D}\left[\frac{6J(|\omega_{\mathrm{H}}|-|\omega_{\mathrm{N}}|) - 5J(\omega_{\mathrm{H}}) - J(|\omega_{\mathrm{H}}|+|\omega_{\mathrm{N}}|)}{J_{\mathrm{eff}}(0)}\right]\right] \tag{25}$$

$$J_{\mathrm{red}}(\omega_{\mathrm{N}}) = J(\omega_{\mathrm{N}})\left[1 - \frac{12}{5}\frac{1}{3 + C/D}\left[\frac{J(|\omega_{\mathrm{H}}|-|\omega_{\mathrm{N}}|) - J(|\omega_{\mathrm{H}}|+|\omega_{\mathrm{N}}|)}{J(\omega_{\mathrm{N}})}\right]\right] \tag{26}$$

$$J_{\mathrm{red}}(|\omega_{\mathrm{H}}|-|\omega_{\mathrm{N}}|) = J(|\omega_{\mathrm{H}}|-|\omega_{\mathrm{N}}|)\left[{}^{6}\!/_{5} - {}^{1}\!/_{5}\left[\frac{J(|\omega_{\mathrm{H}}|+|\omega_{\mathrm{N}}|)}{J(|\omega_{\mathrm{H}}|-|\omega_{\mathrm{N}}|)}\right]\right] \tag{27}$$

Deviations of +10 and −10% are expected of $J_{\mathrm{red}}(|\omega_{\mathrm{H}}|-|\omega_{\mathrm{N}}|)$ from $J(|\omega_{\mathrm{H}}|-|\omega_{\mathrm{N}}|)$ if the ratio $J(|\omega_{\mathrm{H}}|+|\omega_{\mathrm{N}}|)/J(|\omega_{\mathrm{H}}|-|\omega_{\mathrm{N}}|)$ is 0.5 and 1.5, respectively. Note that, for models of motion in which $J(\omega)$ decreases monotonically with ω, $J_{\mathrm{red}}(|\omega_{\mathrm{H}}|-|\omega_{\mathrm{N}}|)$ always overestimates the true $J(|\omega_{\mathrm{H}}|-|\omega_{\mathrm{N}}|)$. The overestimation error is limited to 20% in the event that $J(|\omega_{\mathrm{H}}|+|\omega_{\mathrm{N}}|)/J(|\omega_{\mathrm{H}}|-|\omega_{\mathrm{N}}|)$ goes to 0. The deviations for the higher frequency $J_{\mathrm{red}}(\omega)$ are larger under the same considerations; thus, we identify $J_{\mathrm{red}}^{\mathrm{hifreq}}$ with $J_{\mathrm{red}}(|\omega_{\mathrm{H}}|-|\omega_{\mathrm{N}}|)$, and

$$J_{\mathrm{red}}(|\omega_{\mathrm{H}}|-|\omega_{\mathrm{N}}|) = \frac{1}{5D}R_{\mathrm{N}}(\mathrm{H}_z^{\mathrm{N}} \leftrightarrow \mathrm{N}_z) \tag{28}$$

Generally, the deviations between the full and reduced spectral densities are minor if the actual $J(\omega)$ varies slowly in the neighborhood of $|\omega_{\mathrm{H}}| \pm |\omega_{\mathrm{N}}|$. To examine more rigorously the deviations between the reduced and full spectral density-mapping approaches, one could simulate various spectral density functions and calculate the relaxation rate constants that would ensue. These rate constants could then be used to find the $J_{\mathrm{red}}(\omega)$ values, which would then be compared with the original simulated values. Such a study is reported elsewhere (Lefévre et al., 1996), and the agreement between $J_{\mathrm{red}}(\omega)$ and $J(\omega)$ has been found to be excellent in the cases for which $J(\omega)$ is a decreasing function of ω.

Use of a reduced spectral density-mapping approach has several advantages over the original method proposed. First, only three relaxation rate constants [$R_{\mathrm{N}}(\mathrm{N}_z)$, $R_{\mathrm{N}}(\mathrm{N}_x)$, and $R_{\mathrm{N}}(\mathrm{H}_z^{\mathrm{N}} \leftrightarrow \mathrm{N}_z)$] need to be measured for each B_0. Second, these rate constants are presently easier to measure than those involving proton–proton DD relaxation. Finally, the error propagation properties of eqs 17–19 and 23 are more tolerant of statistical fluctuations in the experimental data. This is illustrated in Figure 5A,B. Using the model form of $J_{\mathrm{ls,ext}}(\omega)$ in eq 20, hypothetical spectral density values were simulated and the relaxation rates calculated. Fractional uncertainties of 5% were then assumed for the fictitious data. $J(\omega)$ and $J_{\mathrm{red}}(\omega)$ values and their associated uncertainties were then computed. The results are shown in Figure 5A,B. In the case of a full spectral density-mapping procedure, huge uncertainties are propagated to the higher frequency $J(\omega)$ values from rather modest error estimates. Drastic overestimation of the true $J(\omega)$ values or even negative $J(\omega)$ values may occur due to random errors alone. In contrast, the errors propagated to the reduced spectral density values are much smaller and are typically on the order (2–5%) of those of the rate constants. Clearly, since the $J_{\rm red}(\omega)$ expressions involve summations of fewer rate constants, their error-propagation properties are more amenable. In particular, the single high-frequency $J(\omega)$ is characterized by a single experimental parameter, $R_N(H_z^N \leftrightarrow N_z)$.

Nonetheless, a clear disadvantage of the reduced mapping procedure is that the possibility of determining the behavior of the spectral density functions in the neighborhood of $|\omega_H| \pm |\omega_N|$ at a single field is lost by virtue of the approximation given in eq 21. However, this disadvantage can be partially compensated for by performing relaxation measurements at multiple fields. For example, one can compare $J_{\rm red}(|\omega_H| - |\omega_N|)$ as a function of B_o. Equation 24 shows that $J_{\rm red}(|\omega_H| - |\omega_N|)$ is directly proportional to $R_N(H_z^N \leftrightarrow N_z)$. Then, if $J(\omega)$ is accurately described as a sum of Lorentzians centered at 0, then $R_N(H_z^N \leftrightarrow N_z)$ should always decrease with increasing B_o. Observation of an enhanced heteronuclear cross-relaxation rate at higher field would therefore rule out the possibility of formulating $J(\omega)$ as a sum of Lorentzians centered at 0.

The eglin c relaxation data at all three fields have also been analyzed using the reduced spectral density formulae of eqs 22–24 and 28. Listings of the reduced spectral density values are provided in the supporting information. Comparisons of the $J_{\rm red}(\omega)$ and $J(\omega)$ values for all residues of eglin c reveals that $J_{\rm red}(0)$ ranges from 0 to 3% larger than $J(0)$ when averaged over all NH bonds. $J_{\rm red}(\omega_N)$ is larger than $J(\omega_N)$ by 3 to 20%. In both cases, the smallest deviations are made by the 7.04 T measurements. The results of the reduced mapping approach for the same four representative residues of Phe3, Arg22, Asp46, and Arg53 are shown in Figure 6A–D. Due to eq 24, all $J(\omega)$ values are positive. Additionally, the three higher frequency $J_{\rm red}(\omega)$ values decrease with increasing frequency; this was foreshadowed by the fact that $R_N(H_z^N \leftrightarrow N_z)$ decreased with increasing B_o. Thus, the description of the NH spectral densities in terms of a series of Lorentzians centered at $\omega = 0$ is a reasonable one. The smaller error bars emphasize the marked increase in precision inherent in the reduced mapping approach. The compensatory behavior expected in the high-frequency spectral density values is also more clearly demonstrated by the reduced mapping approach. This is illustrated by a comparison of Figure 7A–C, which plots $J_{\rm red}(|\omega_H| \pm |\omega_N|)$ as a function of protein sequence, with the $J(0)$ and $J(\omega_N)$ plots in Figure 3. Residues with significantly low $J_{\rm red,eff}(0)$ and $J(\omega_N)$ have elevated $J_{\rm red}(|\omega_H| - |\omega_N|)$. The experimental confirmation of the expected compensatory behavior is due, again, to the direct proportionality of $J_{\rm red}(|\omega_H| \pm |\omega_N|)$ with $R_N(H_z^N \leftrightarrow N_z)$. Figure 7A–C also confirms that relaxation measurements at 7.04 T show the least discrepancy between $J_{\rm red}(|\omega_H| \pm |\omega_N|)$ and $J(|\omega_H| \pm |\omega_N|)$.

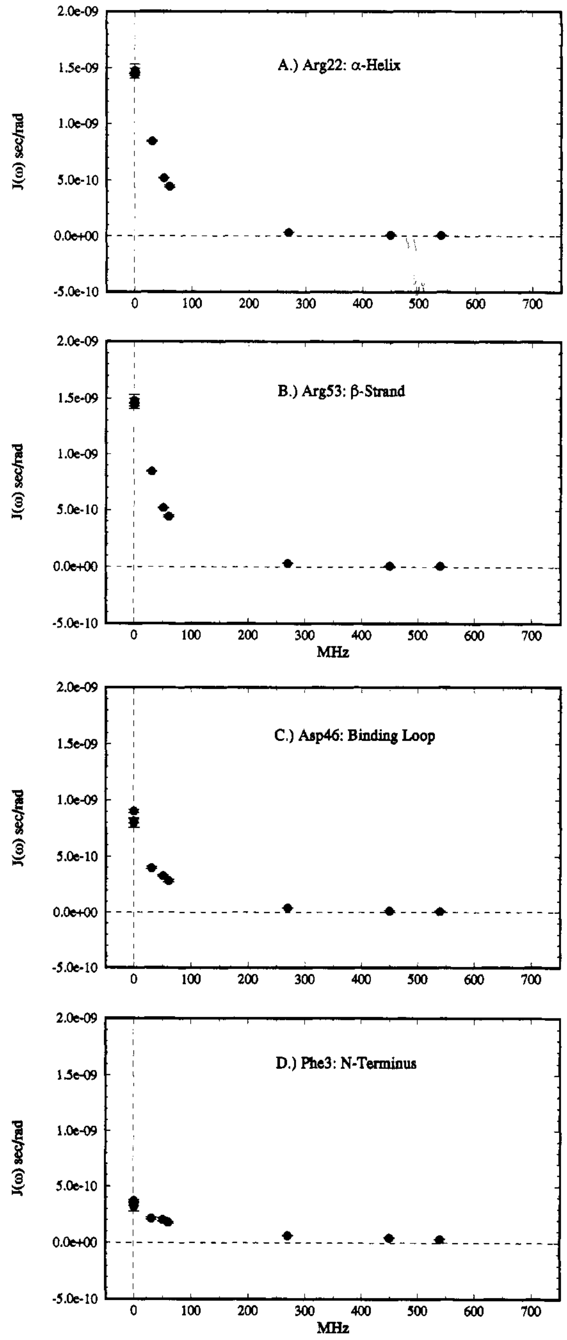

FIGURE 6: Reduced spectral density profiles resulting from the relaxation measurements at 7.04, 11.74, and 14.1 T for the amide NH bonds of (A) Arg22, (B) Arg53, (C) Asp46, and (D) Phe3. Equations 22–24 in the text were used to extract nine spectral density values (seven unique) for each NH bond.

Influence of Chemical Exchange. The NH bond vector dynamics may involve both reorientation and exchange processes. If the exchange processes modulate the ^{15}N chemical shift, then the transverse relaxation rate constants will have an $R_{\rm ex}$ contribution (eqs 2 and 3). Furthermore, the observed zero-frequency sampling of the spectral density function, $J_{\rm eff}(0)$, will be greater than $J(0)$ (cf. eq 9). The presence of exchange processes may be revealed by anomalously fast transverse relaxation rates, resulting in spuriously large $J_{\rm eff}(0)$ values. However, if NH bonds also experience fast internal motions, then the exchange processes may not be so easily targeted. A comparison of $J_{\rm eff}(0)$ values at different B_o strengths provides an alternative means of screening the relaxation data for $R_{\rm ex}$ contributions. Since $R_{\rm ex}$ scales as the square of the ω_N Larmor frequency, we can write $R_{\rm ex} = \Phi\omega_N^2$. The proportionality factor Φ depends on parameters including the number and population of the hypothetical exchange sites, the corresponding chemical shift differences, and the rate constants governing the exchange. Φ is then derived from $J_{\rm eff}(0)$ at two B_o fields (field$_1$ and

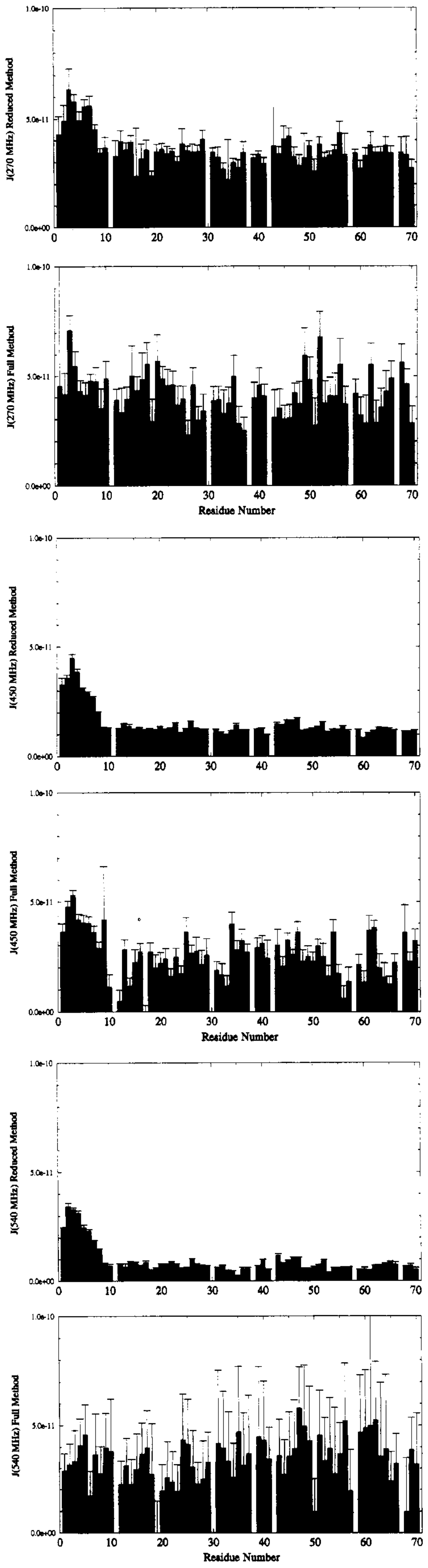

FIGURE 7: Comparison of $J_{\mathrm{red}}(|\omega_H|-|\omega_N|)$ (top) and $J(|\omega_H|-|\omega_N|)$ versus protein sequence. The values clearly decrease in the case of $J_{\mathrm{red}}(|\omega_H|-|\omega_N|)$. Additionally, the relative increase of the values for the first eight NH bonds becomes more pronounced at higher frequencies.

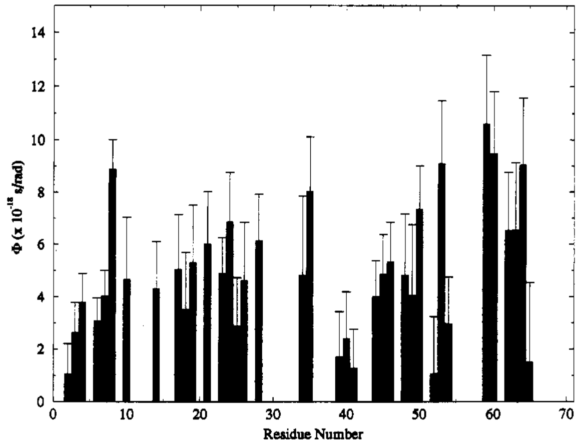

FIGURE 8: Exchange parameter Φ versus protein sequence. The Φ values are obtained by fitting $J_{\mathrm{eff,red}}(0)$ to eq 30 in the text. Blank slots indicate NH bonds for which an increase of $J_{\mathrm{eff,red}}(0)$ with B_o could not be observed.

field$_2$) via the ratio

$$\Phi = [J_{\mathrm{eff},1}(0) - J_{\mathrm{eff},2}(0)]/(\lambda_1\omega_{\mathrm{N},1}^2 - \lambda_2\omega_{\mathrm{N},2}^2) \quad (29)$$

λ_1 and λ_2 are the same λ factors first shown in eq 15 for the two field strengths denoted by subscripts 1 and 2. Alternatively, if $J_{\mathrm{eff}}(0)$ values are available from more than two fields, then they may simply be fit to the form given by eq 9 which is repeated here as

$$J_{\mathrm{eff}}(0;\, \omega_N) = J(0) + \lambda(\omega_N)\omega_N^2\Phi \quad (30)$$

$J(0)$ is field independent, and λ itself depends on ω_N^2 through the CSA factor C. As stated previously, there is no striking evidence for NH exchange dynamics in eglin c in the form of dramatically enhanced transverse relaxation rates. Accordingly, the eglin c $J_{\mathrm{eff,red}}(0)$ values have been fitted to the form of eq 30. A plot of the Φ values versus protein sequence is given in Figure 8. Blank slots indicate residues for which a monotonic increase of $J_{\mathrm{eff,red}}(0)$ was not observed. Rather unexpectedly, small monotonic increases of $J_{\mathrm{eff,red}}(0)$ with B_o are observed for slightly over half of the NH resonances, with typical values ranging between 1.0×10^{-18} and 5.0×10^{-18} s/rad. This suggests the presence of wide spread exchange processes for eglin c. However, the typical fractional uncertainties in these Φ values is between 30 and 40%. Additionally, the range of R_{ex} contributions that would arise from these Φ values ($\approx$0.04−0.7 s^{-1} using the relation $R_{\mathrm{ex}} = \Phi\omega_N^2$) well overlaps the range of estimated uncertainties in the transverse relaxation rate constants ($\approx$0.1−0.4 s^{-1}). Accordingly, the significance of these Φ values is presently unclear. The plenitude of small Φ values could be indicative of an unidentified global exchange process, such as that due to protein aggregation. On the other hand, the Φ values could reflect an artifact from a presently unaccounted for field dependence in the relaxation rates. For the latter possibility, one is naturally led to suspect errors in the transverse relaxation rate measurements which dominate the $J_{\mathrm{eff}}(0)$ calculations. Strictly speaking, the experiments used to measure the transverse relaxation rates are $R_{1\rho} = 1/T_{1\rho}$ experiments, and one might suspect the approximation of $R_{1\rho,\mathrm{N}}(\mathrm{N}_x) = R_\mathrm{N}(\mathrm{N}_x)$ to cause an illusory increase of $J_{\mathrm{eff}}(0)$ with B_o. Unfortunately, the additional B_o dependencies introduced by rigorously treating $R_\mathrm{N}(\mathrm{N}_x)$ as $R_{1\rho,\mathrm{N}}(\mathrm{N}_x)$ would seem to decrease $J_{\mathrm{eff}}(0)$ with stronger B_o. Specifically, the use of a fixed spin lock field strength (viz. 2500 Hz) at progressively stronger B_o would progressively decrease the tip angle of the effective field. As a result, the ^{15}N resonances would be spin-locked along axes having a progressively larger z-component, and the observed rate constant would be expected to decrease, and not increase, with stronger B_o [see, for example, Peng and Wagner (1994a,b) and Davis et al. (1994)]. This assertion assumes that any initial ^{15}N magnetization perpendicular to the effective field has already decayed away due to rf inhomogeneity, and therefore, one is only monitoring the decay of magnetization along the effective field axis. Artifacts from resonance offset effects are also difficult to envision since one does not see a clear correlation between resonance offset and the increasing $J_{\rm eff}(0)$ values. For example, Ser9 and Phe25 have ostensibly the same offset from the ^{15}N carrier in all experiments. Yet, $J_{\rm eff,red}(0)$ remains essentially invariant for Ser9, while it shows a monotonic increase for Phe25. More unexpectedly, the NH residues that typically show the largest $R_N(N_x)$ values (Glu12, Val13, and Arg51) at all field strengths do not show a systematic increase with B_o. It is possible that the expected increase is quenched by off-resonance effects during the ^{15}N spin lock. While this is plausible for the NH bonds of Val13 and Arg51, it is less plausible in the case of Glu12, whose amide ^{15}N chemical shift lies essentially on the ^{15}N carrier. Thus, the larger transverse relaxation rate constants for this NH bond may reflect high restriction of internal motion, as opposed to chemical exchange effects.

The strongest cases for exchange include the NH bonds of Lys8, Arg53, Gly59, Thr60, and Asn64. These bonds display the largest systematic increases of $J_{\rm eff,red}(0)$ with B_o. The parameter Φ is 8.98 ± 1.15 ($\times 10^{-18}$ s/rad) for Lys8, 9.11 ± 2.4 ($\times 10^{-18}$ s/rad) for Arg53, 10.7 ± 2.6 ($\times 10^{-18}$ s/rad) for Gly59, 9.51 ± 2.37 ($\times 10^{-18}$ s/rad) for Thr60, and 9.09 ± 2.56 ($\times 10^{-18}$ s/rad) for Asn64. Thus, these Φ values have typical fractional uncertainties of 25% and result in $R_{\rm ex}$ contributions of approximately 0.3 to 1.4 s^{-1} as one moves from 7.04 to 14.1 T. Additionally, the maximal $R_{\rm ex}$ contributions are outside of the typical estimated errors for the transverse relaxation rates. The possibility of exchange processes at these sites corroborates well with earlier NMR studies of eglin c (Hyberts & Wagner, 1990; Hyberts et al., 1992). In particular, the NH bonds of Gly59 and Thr60 lie within a type I turn defined by Pro58-Gly59-Thr60-Asn61. This turn displays a relatively higher spread of dihedral angles in the solution structure calculations (Hyberts et al., 1992). Additionally, the proton−deuteron exchange rates of the Gly59 and Thr60 amide protons are also relatively enhanced from the majority of residues (vida infra). Thus, the Φ factors for these residues may reflect local conformational fluctuations of this turn. Similarly, the NH bonds of Asn64 and Lys8 have enhanced amide proton exchange rates and lie near regions of poor structural precision. Asn64 precedes a β-bulge, while Lys8 is just after the highly flexible N-terminal heptapeptide. An explanation for the Arg53 Φ factor is less obvious. Arg53 resides in the midst of a β-strand defined by Asn50−Tyr56, and its side chain helps stabilize the binding loop conformation (Hipler et al., 1992) through intramolecular hydrogen bonds. The large Φ value for Arg53 suggests that the buttressing for the flexible binding loop may also be flexible, albeit, on a much longer time scale. One possibility is that the four-stranded β-sheet in which Arg53 participates has some internal flexibility. The crystal structure of chymostrypsin inibitor 2 (CI2), which has a different primary sequence but is structurally and functionaly very similar to eglin c, may provide insight here (McPhalen & James, 1987). Specifically, the crystal structure reveals that the analogous four-stranded β-sheet of CI2 actually consists of two pairs of β-strands that are indirectly joined via hydrogen bonds to five water molecules that lie between the two sets of strands. The NH of the CI2 arginine analogous to Arg53 has a hydrogen bond to one of these structural waters (McPhalen & James, 1987). The water-mediated linkage between the two sets of β-strands in CI2 may lend enhanced internal flexibility to the β-sheet. Such a flexible β-sheet might also exist for eglin c, leading to the chemical exchange effects seen for Arg53. Accordingly, work to identify close contacts between Arg53 and structural water molecules via 2D NOE and ROE experiments is in progress.

It is clear that Φ and $R_{\rm ex}$ do not directly give exchange time constants. The extraction of time constants from these quantities requires a model form for $J_{\rm exch}(\omega)$, which denotes the spectral density describing the putative exchange processes. This, in turn, demands assumptions about the number of exchanging states, their relative populations, and the chemical shift differences involved. Moreover, use of ^{15}N spin locks for the transverse relaxation experiments complicates the analytical forms for Φ and $R_{\rm ex}$ with terms involving the resonance offset and spin lock field strength. Nonetheless, to obtain a rough estimate of time scales, we can assume a simple two-state exchange process and neglect all spin lock considerations. Then $\Phi = p_a p_b(\Delta\delta)^2\tau_{\rm ex}$, where p_a and p_b are the fractional populations of the two states, $\Delta\delta$ is the ^{15}N chemical shift difference in parts per million, and $\tau_{\rm ex}$ is the exchange constant (Deverell et al., 1970; Wennerström, 1972). If we assume $\Delta\delta = 1$ ppm, $p_a = p_b = 0.5$, and $1.0\ {\rm s}^{-1} < R_{\rm ex} < 1.4\ {\rm s}^{-1}$ at 14.1 T, then $\tau_{\rm ex}$ lies in the range $28\ \mu{\rm s} < \tau_{\rm ex} < 40\ \mu{\rm s}$. As stated, such dynamic processes are much slower than those governing the orientational fluctuations of the NH bonds described by the $J(\omega)$ functions alone.

To circumvent the above difficulties in identifying $\tau_{\rm ex}$, one can perform ^{15}N $R_{1\rho}$ experiments as a function of variable spin lock field strength, here designated by B_1. If the rate constants for exchange ($1/\tau_{\rm ex}$) are comparable to applied $\gamma_N B_1$, then the relaxation rates display an attenuation with increasing B_1 (Deverell et al., 1970; Wennerström, 1972; Szyperski et al., 1993; Davis et al., 1994; Nicholson et al., 1995). A fit of the $R_{1\rho}$ dispersion with B_1 to a model $J_{\rm exch}(\omega)$ function permits the extraction of an exchange time constant. Such studies have been attempted for eglin c at 11.74 T. Thus far, no significant dependence upon the ^{15}N spin lock field strength, B_1, has been observed. Thus, from the ^{15}N $R_{1\rho}$ study alone, one fails to identify any exchange processes in eglin c. This failure is not surprising, given that $R_{1\rho}$ can lose its sensitivity to exchange processes if the chemical shift differences are very small, if populations of exchanging states are very lopsided, or if the exchange rates exceed the maximal B_1 strength available. In the studies performed thus far at $B_o = 11.74$ T, we have been limited to a maximum spin lock strength of $\gamma_N B_1/2\pi = 2970$ Hz. Note that, if the above estimates of $\tau_{\rm ex} \approx 40\ \mu$s are reasonable, we would require a $\gamma_N B_1/2\pi$ strength of nearly 4000 Hz for strong $R_{1\rho}$ dispersion. Thus, mapping $J_{\rm eff,red}(0)$

at variable B_o, although being more laborious, offers an alternative means for identifying chemical exchange processes in instances when an $R_{1\rho}$ study proves insensitive or not feasible.

Interpretation of the Spectral Density Values Using Motional Models. A comparison of the reduced and full $J(\omega)$ values as a function of frequency and protein sequence allows regions of enhanced internal mobility to be identified. Such identifications can be made without any *a priori* assumptions about the atomic motion.

To further describe this mobility in terms of specific types of motion (e.g. bond wobbling, site hopping, helix rolling, etc.) requires use of a specific model of motion. Such models prescribe analytical forms for $J(\omega)$ that are derived from certain assumptions concerning the orientational autocorrelation function describing the NH bond dynamics. Spectral density mapping allows direct comparison between experimental spectral density values and those predicted by such model forms.

The $J_{\rm ls}(\omega)$ model form of eq 17 was used to fit the experimental $J_{\rm red}(\omega)$ and $J(\omega)$ profiles, and the resulting values for S^2 and $\tau_{\rm i}$ are summarized in the supporting information. The protocol used in the model-fitting procedure is essentially the same as that outlined previously (Peng & Wagner, 1992b), except that the spectral density values themselves are directly fit instead of the rate constants. Additionally, to account for the possible effects of exchange broadening, the fitted value of $J(0)$ in eq 30 has been used for only those residues showing a monotonic increase of $J_{\rm eff}(0)$ with B_o. Clearly, the degree of accuracy in these extrapolated $J(0)$ values can strongly affect the agreement between the model $J_{\rm ls}(\omega)$ functions and the experimental values. Erroneously small or larger $J(0)$ values lead to broader or narrower $J_{\rm ls}(\omega)$ distributions, respectively. Such erroneously biased distributions might then be incompatible with the experimental spectral density values at higher frequencies.

Fits of the reduced spectral density values $J_{\rm red,eff}(0)$, $J_{\rm red}(\omega_{\rm N})$, and $J_{\rm red}(|\omega_{\rm H}|-|\omega_{\rm N}|)$ (nine values per NH bond) yield an optimal overall correlation time of $\tau_{\rm rot} = 3.85 \pm 0.1$ ns/rad. This is slightly less than the value of 4.1 ns/rad obtained from the 11.74 T data alone. The average S^2, excluding the more mobile N-terminal residues and binding loop residues, is 0.82. The $\tau_{\rm i}$ values have an average value of less than 20 ps/rad. The average uncertainties in S^2 and $\tau_{\rm i}$ are ±0.008 and ±18 ps/rad, respectively. These results are essentially the same as seen previously (Peng & Wagner, 1992b). Residues of reduced S^2 correspond to those with lower $J(0)$ values. This is reasonable, given that $J_{\rm ls}(0) = S^2\tau_{\rm rot} + (1 - S^2)\tau_{\rm e}$ and that $\tau_{\rm e}$ is typically much less than $\tau_{\rm rot}$. Examples of the fits between $J_{\rm ls}(\omega)$ and $J_{\rm red}(\omega)$ are given by the dashed traces in Figure 9A–D for Phe3, Asp46, Arg22, and Arg53.

Fits of the spectral density values from the full mapping approach of eqs 9–14 have also been performed [15 $J(\omega)$ points per NH bond]. While the relative variations of the S^2 and $\tau_{\rm i}$ parameters as a function of protein sequence are similar to those found using the $J_{\rm red}(\omega)$ values, the average values are changed. Additionally, the estimated uncertainties in the fitted parameters are noticeably larger. In particular, one finds an optimal $\tau_{\rm rot}$ of 4.3 ± 0.4 ns/rad. The core residue average S^2 and uncertainty in S^2 are 0.71 and ±0.1, respectively. The core residues' average $\tau_{\rm i}$ and uncertainty in $\tau_{\rm i}$ are 570 and ±520 ps/rad, respectively. These differences are most likely artifacts of the fitting protocol trying to cope with the unexpectedly large high-frequency $J(\omega)$ values, especially those emanating from the 14.1 T data. Large positive excursions at high frequencies lead to large $\tau_{\rm i}$ values and lower S^2 values. In order to simultaneously fit the low-frequency data, the fitting procedures which increase the overall tumbling time, $\tau_{\rm rot}$, must therefore increase.

The necessity of $J_{\rm ls,ext}(\omega)$ (eq 20) was also investigated. The optimized parameters of $J_{\rm ls}(\omega)$ were used as starting

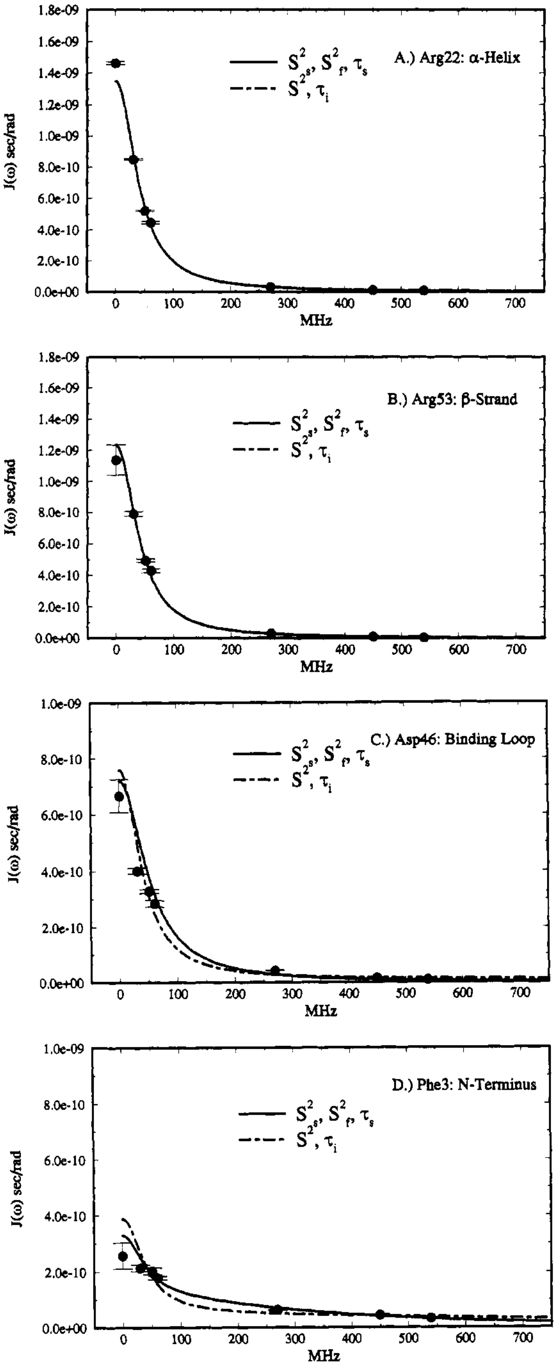

FIGURE 9: Fits of the experimental $J_{\rm red}(\omega)$ to the model spectral density functions given in eqs 17 and 20 for (A) Arg22, (B) Arg53, (C) Asp46, and (D) Phe3. The dashed lines indicate fits to $J_{\rm ls}(\omega)$ (eq 17 in the text). The solid lines indicate fits to $J_{\rm ls,ext}(\omega)$ (eq 20 in the text). For both fits, the overall rotational correlation time, $\tau_{\rm rot}$, is 3.85 ± 0.1 ns/rad. For the $J_{\rm ls,ext}(\omega)$ fits, the subscripts s and f indicate slow and fast, respectively. Phe3 (C) and Asp46 (D) show differences between the $J_{\rm ls}(\omega)$ and $J_{\rm ls,ext}(\omega)$ fits, whereas essentially no differences are seen for Arg22 (A) and Arg53 (B).

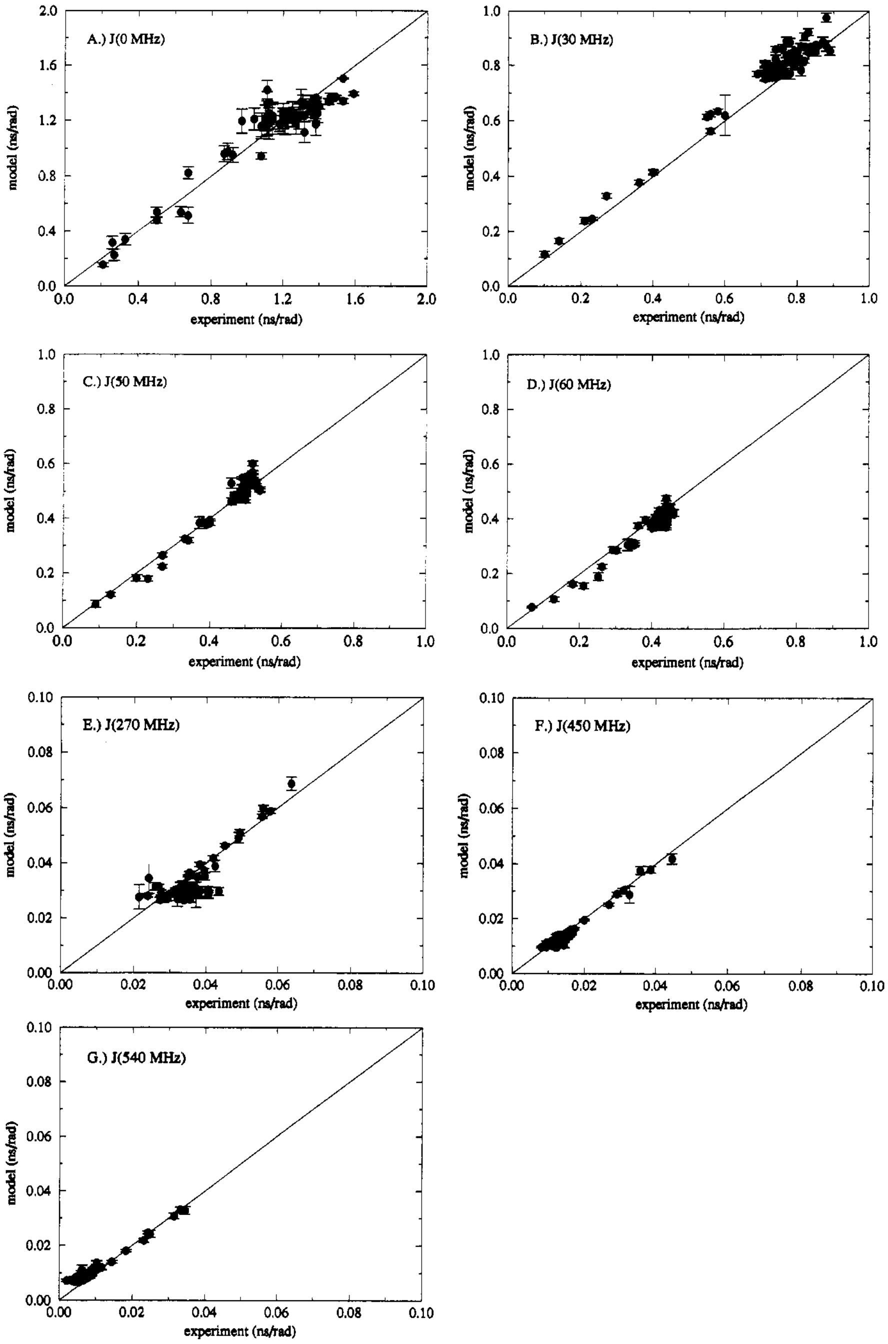

FIGURE 10: Plots of the experimental reduced spectral density values (abscissa) versus those obtained by fitting the spectral density data to the Lipari–Szabo model forms (ordinate) at (A) 0, (B) 30, (C) 50, (D) 60, (E) 270, (F) 450, and (G) 540 MHz. The plots are in units of nanoseconds per radius. The dense clusters of dots in all figures correspond to NH bonds located in the core of eglin c, while the tails of the dots correspond to NH bonds in the flexible N-terminus and protease binding loop.

conditions for the fitting of the $J_{\mathrm{red}}(\omega)$ data to $J_{\mathrm{ls,ext}}(\omega)$. Minor fitting improvements were made in the N-terminal residues using S_f^2 values of ≈0.71–0.8. However, for the remainder of the protein backbone, no significant improvements were observed using the extended model. The specific values of S_f^2 are also included in the supporting information. Examples of the fits are indicated by the solid traces in Figure 9A–D. Note that, for Arg22 and Arg53, the fit lies essentially on top of that produced by the simpler $J_{\mathrm{ls}}(\omega)$ (eq 17) and is therefore not visible.

While the fits between eq 20 and the reduced spectral density data appear qualitatively good, there are a number of systematic deviations that should be pointed out. For example, the observed decrease of $J_{\mathrm{red}}(\omega_{\mathrm{N}})$ with frequency is slower than that predicted by the model forms of $J(\omega)$. This manifests as a consistent overestimation of J_{red}(30 MHz) and an underestimation of J_{red}(60 MHz). The fitting procedure tends to fit J_{red}(50 MHz) rather well, since its value lies between J_{red}(30 MHz) and J_{red}(60 MHz). At $J_{\mathrm{red}}(|\omega_{\mathrm{H}}| - |\omega_{\mathrm{N}}|)$, the high frequency, the problem is reversed. Here, J_{red}(270 MHz) tends to be underestimated by the model parameters, whereas J_{red}(540 MHz) is overestimated. Thus, at high frequencies, the measured spectral density function decreases faster than the model spectral density function. In Figure 10A–G, these trends are illustrated by plots of the experimental spectral density values against their model counterparts. The dots have abscissas and ordinates corresponding to the experimental and model values, respectively.

In all panels, the residues of the more rigid core cluster together while residues of the more flexible parts stretch out along the diagonal at lower values for $J(0)$ and $J(\omega_N)$, and at higher values for $J_{red}(|\omega_H|-|\omega_N|)$. The small discrepancies described may point to an inadequacy of the proposed model form for the spectral density function or to systematic errors in the experimental data. It is worth recalling that the model forms of eqs 17 and 20 assume the simplest case of isotropic overall tumbling for the protein molecule. In fact, the overall shape of eglin c is that of a slightly oblate ellipsoid, and therefore, the assumption of isotropic tumbling is not *a priori* rigorously correct. Note that the deviations between the relaxation parameters from an oblate ellipsoid and those from a sphere are not expected to be severe (Schleich et al., 1989). Nonetheless, it is possible that better fits between the experimental and model spectral density functions could be obtained by allowing for the possibility of a residual anisotropy in molecular tumbling. If we exclude the possibility that the model spectral densities of eqs 17 and 20 are unable to model the experimental spectral densities, then we must look for potential systematic errors in the experimental parameters. Equations 22–24 show that the accuracy of $J_{red}(\omega_N)$ and $J_{red}(|\omega_H|-|\omega_N|)$ depends upon accurate measurements of $R_N(N_z)$ and the heteronuclear cross-relaxation rate constant, $R_N(H_z^N \leftrightarrow N_z)$. An underestimation of the latter rate would produce the observed overestimation of $J_{red}(\omega_N)$ and an underestimation of $J_{red}(|\omega_H|-|\omega_N|)$. Erroneously small values of $R_N(H_z^N \leftrightarrow N_z)$ can result from the use of solvent presaturation (Neuhaus & van Mierlo, 1992; Skelton et al., 1993; Li & Montelione, 1994), as in the present work. However, this effect is expected to be pronounced only for a limited number of residues experiencing rapid amide proton exchange and not the majority of backbone NH bonds. Indeed, as the present study was carried out at pH = 3.0, it is not clear that presaturation effects are the main culprit. Moreover, any proposal for a systematic underestimation of $R_N(H_z^N \leftrightarrow N_z)$ must predict an underestimation that exacerbates with stronger B_0. For example, incomplete saturation of the amide protons during the heteronuclear NOE experiments would also yield underestimates of $R_N(H_z^N \leftrightarrow N_z)$. It is possible that increasingly incomplete proton saturation with stronger B_0 could cause progressively larger underestimates of $R_N(H_z^N \leftrightarrow N_z)$. At this point, however, it seems that the discrepancies between the experimentally determined values of the spectral density function and the fit to the Lipari–Szabo model functions (eqs 17 and 20) are not due to experimental errors. It is possible that directly fitting a sum of Lorentzians rather than the Lipari–Szabo parameters would produce a better agreement. Another potential source of small discrepancies is the simplifying assumption that the NH bond distance and the ^{15}N CSA are the same for all NH bonds. Recall that eqs 9–13 and 22–24 used to derive the spectral density values contain the D and C parameters, which depend on the NH bond distance and ^{15}N CSA, respectively. These parameters effectively scale the $J(\omega)$ values. Thus, it is conceivable that the assumption of constant NH bond length and ^{15}N CSA could produce small errors in the resulting spectral density values. Accordingly, the use of more site-specific ^{15}N CSA values and NH bond lengths might also improve the agreement between experimental and model $J(\omega)$ values. New ways to measure individual CSA values via relaxation measurements (e.g. for carbonyl carbons) are currently under investigation (K. T. Dayie and G. Wagner, manuscript in preparation).

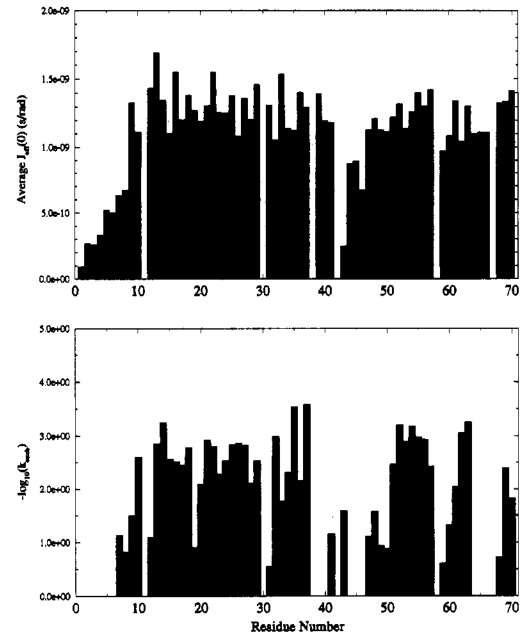

FIGURE 11: Amide proton–deuteron exchange rates measured at 11.74 T in comparison with $J(0)$ values as a function of protein sequence. Exchange rates are quoted in $-\log(k_m)$, where k_m is the apparent first order rate constant. $J(0)$ values are averaged over the three spectrometer fields.

Comparison with Amide Hydrogen–Deuteron Exchange Rate Constants. It is of further interest to compare the $J(\omega)$ values with the amide proton–deuteron exchange rate constants. Figure 11 depicts the average $J_{eff,red}(0)$ and the negative log of the H–D exchange rate constants, k_m, as a function of protein sequence. Tall bars on the exchange plot indicate small k_m values and therefore slow amide exchange. In total, it was possible to measure 49 out of 64 possible NH exchange rates. A list of the exchange rate constants and the ^{15}N chemical shifts are given in Table 2. The rates vary from 0.26×10^{-3} to 284×10^{-3} min^{-1}. The slowest exchanging amides are involved in β-strands, and the fastest exchanging amides are those which are not within regular secondary structure. Blank slots in exchange plots indicate prolines or residues with amide protons that exchange completely within 10 min. NH protons of the latter class include those of the N-terminal residues, residues 39 and 40, the proteinase binding loop residues 44–46, and the residues within the β-bulge, 64–66. Comparison of the two bar graphs shows that regions of low $J(0)$ (fast NH vector reorientation) are also regions or rapid H–D exchange. However, regions of rapid H–D exchange are not necessarily regions of low $J_{eff,red}(0)$. The NH bonds of the β-bulge residues Asn64 and Val66 clearly illustrate this. The lack of correspondence is most likely due to the vastly different time scales of dynamics probed by $J_{eff,red}(0)$ and k_m. Whereas the presence of fast internal fluctuations indicated by attenuated $J_{eff,red}(0)$ may predispose an NH toward rapid H–D exchange, slower conformational fluctuations that allow rapid H–D exchange need not necessarily predispose the NH vector toward faster reorientational motions. Similar results have been reported by Kördel et al. in the ^{15}N dynamics studies of calbindin D_{9k} (Kördel et al., 1992).

Table 2: ^{15}N and ^{1}H Chemical Shifts and Amide Proton Exchange Rate Constants for Eglin C (pH = 3, $T = 36$ °C)[a–d]

NH	^{15}N (ppm)	^{1}H (ppm)	k_{ex} ($\times 10^{-3}$ min^{-1})
Thr1	118.93	8.10	–
Glu2	121.86	8.32	–
Phe3	120.32	8.17	–
Gly4	109.69	8.22	–
Ser5	114.93	8.10	–
Glu6	120.78	8.27	–
Leu7	122.86	8.07	73.720 (9.931)
Lys8	123.71	7.89	152.800 (5.911)
Ser9	117.01	7.89	31.970 (0.297)
Phe10	113.92	7.66	2.541 (0.015)
Glu12	118.39	9.53	80.930 (2.407)
Val13	110.30	7.09	1.413 (0.009)
Val14	120.48	7.18	0.566 (0.004)
Gly15	115.39	9.10	2.783 (0.018)
Lys16	119.63	7.84	3.070 (0.019)
Thr17	109.69	8.43	3.636 (0.024)
Val18	120.09	8.07	1.685 (0.012)
Asp19	116.01	8.39	127.700 (4.260)
Gln20	119.17	7.70	8.186 (0.053)
Ala21	124.25	9.39	1.212 (0.007)
Arg22	119.94	9.06	1.605 (0.008)
Glu23	118.70	7.59	5.265 (0.031)
Tyr24	119.40	8.11	2.995 (0.028)
Phe25	117.39	8.62	1.485 (0.014)
Thr26	115.62	8.30	1.395 (0.009)
Leu27	116.39	7.74	1.494 (0.009)
His28	111.30	7.80	7.934 (0.074)
Tyr29	117.01	8.38	2.987 (0.028)
Gln31	118.16	9.53	283.800 (26.240)
Tyr32	119.01	7.35	1.034 (0.011)
Asp33	119.94	9.04	17.200 (0.169)
Val34	125.33	8.10	4.898 (0.036)
Tyr35	125.56	8.23	0.287 (0.004)
Phe36	121.71	8.84	7.033 (0.057)
Leu37	126.79	9.25	0.261 (0.005)
Glu39	122.71	8.82	–
Gly40	112.46	8.67	–
Ser41	117.16	7.72	68.860 (1.078)
Val43*	115.23	8.07	25.510 (0.249)
Thr44	112.85	7.66	–
Leu45	123.10	8.60	–
Asp46	118.78	8.16	–
Leu47	122.09	8.13	79.360 (3.096)
Arg48	126.10	8.82	26.220 (0.265)
Tyr49	120.24	8.46	115.700 (3.214)
Asn50	114.00	8.37	132.900 (5.480)
Arg51	121.86	7.29	3.464 (0.023)
Val52	122.56	8.37	0.626 (0.005)
Arg53	126.49	8.62	1.280 (0.012)
Val54	124.64	8.69	0.671 (0.009)
Phe55	126.41	9.21	1.063 (0.010)
Tyr56*	115.39	8.13	1.174 (0.012)
Asn57	121.71	8.60	3.814 (0.029)
Gly59	106.29	8.54	249.500 (22.500)
Thr60	107.30	7.28	47.850 (0.862)
Asn61	116.39	8.89	9.098 (0.098)
Val62	115.54	7.41	0.881 (0.006)
Val63	126.87	8.87	0.553 (0.005)
Asn64	126.87	8.91	–
His65	115.31	7.77	–
Val66	126.02	9.17	0.000 (0.000)
His68	116.39	8.82	191.000 (21.460)
Val69	121.01	8.53	4.091 (0.024)
Gly70*	121.71	8.84	15.380 (0.146)

[a] Amide ^{15}N chemical shifts are referenced to $NH_4{}^{15}NO_2$ in D_2O. The $NH_4{}^{15}NO_2$ line was taken to be 376.25 ppm at 36 °C. [b] Amide ^{1}H assignments are from Hyberts and Wagner (1990). [c] Amide exchange rates were measured at 11.74 T. Dashes indicate NH resonances that were not detectable after the first 10 min of immersion into D_2O. [d] Asterisks indicate resonances experiencing overlap in the H_2O 2D $^{15}N-^{1}H$ spectra. Tyr56 no longer suffers overlap from Val43 in the exchange spectra, and therefore, the reported rate is meaningful.

CONCLUSIONS

Application of the spectral density-mapping technique at three field strengths to eglin c has permitted an extremely detailed investigation of the frequency spectrum for the NH bond motions. The results show that dynamic heterogeneity along the protein backbone appears most visibly in lower frequency spectral density values (<100 MHz). The presence of enhanced internal mobility on time scales faster than overall molecular tumbling manifests as reductions of these low-frequency spectral density values.

Here we have presented a thorough investigation of the potential for multiple ^{15}N relaxation parameters to characterize the frequency spectrum of motions for the NH bonds. Of course, if one seeks a more qualitative overview of the protein backbone mobility, then a considerably smaller relaxation data base can be used. For example, it has been recently demonstrated that measurement of $R_N(N_z)$ and $R_N(N_x)$ at a single field strength can reliably yield Lipari–Szabo order parameters (S^2) in cases where the internal motion time constant, τ_i, is faster than the overall tumbling time, τ_{rot} (Habazettl & Wagner, 1995), and thereby provide a means for spotting NH bonds experiencing rapid internal motions. Measurements of $R_N(N_x)$ at an additional field strength could then complement these measurements to pinpoint sites of slower conformation exchange. Indeed, the sufficiency of using a smaller data base to characterize backbone mobility is further justified by the in-depth study performed here.

The experimental parameter, $J_{eff}(0) = J(0) + \lambda R_{ex}$ (cf. eq 9), appears to be the most sensitive probe of internal flexibility. This is due to its sensitivity to dynamics processes operating on both slow and fast time scales. Rapid internal reorientations of the NH bonds reduce $J(0)$ and thereby reduce $J_{eff}(0)$. Anomalously low $J_{eff}(0)$ values along the protein sequence therefore indicate enhanced internal mobility on time scales faster than overall molecular tumbling (nanoseconds to sub-nanoseconds). Slower chemical exchange processes that modulate the chemical shift produce the R_{ex} contribution in eq 9 and therefore increase $J_{eff}(0)$. Anomalously large $J_{eff}(0)$ values along the protein sequence may thus indicate slow conformational exchange. While the exchange processes are much slower than the reorientational fluctuations affecting $J_{eff}(0)$, they still involve time constants in the millisecond to microsecond regime such that only a single set of $^{15}N-^{1}H$ correlation peaks are seen (fast exchange regime). Fast and slow motions alter $J_{eff}(0)$ in opposite senses, and thus, the presence of exchange need not always be signified by deviantly large $J_{eff}(0)$ values. To disentangle the exchange contributions to $J_{eff}(0)$, $J_{eff}(0)$ can be obtained at different field strengths. Additionally, examination of the $J(\omega_N)$ spectral density values as a function of protein sequence can also help distinguish between the effects of rapid internal reorientational fluctuations and chemical exchange in $J_{eff}(0)$. Note that R_{ex} is proportional to the zero-frequency value of the exchange spectral density function, $J_{exch}(\omega)$. Heteronuclear $R_{1\rho}$ experiments at different B_1 field strengths may permit a more detailed characterization of this latter spectral density (Peng et al., 1991a,b; Szyperski et al., 1993). Nonetheless, the effectiveness of the $R_{1\rho}$ measurements relies on exchange processes having characteristic time scales on the order of $1/\gamma_N B_1$. Thus, an analysis of $J_{eff}(0)$ versus B_0 can help identify exchange processes that may fail to meet the foregoing criterion.

In principle, the spectral density method permits characterization of $J(\omega_H)$ and $J(|\omega_H|\pm|\omega_N|)$. In practice, these high-frequency $J(\omega)$ values are difficult to determine due to their sensitivity to small errors (statistical or systematic) in the relaxation rate constants. Relaxation measurements on deuterated samples or the use of cross-relaxation-compensated pulse sequences may help reduce the effects of systematic errors. However, a quicker expedient is the use of a reduced spectral density-mapping procedure (Farrow et al., 1995; Lefévre et al., 1996). The errors made by the reduced values when compared to the rigorous values are expected to be small in the event that $J(\omega)$ varies slowly in the neighborhood of ω_H or is small compared to $J(0)$ and $J(\omega_N)$. Use of the reduced mapping approach at several fields allows one to retain the possibility of determining the shape of $J(\omega)$ at high frequencies. Furthermore, use of the reduced approach shows a clear anticorrelation between reduced $J(0)$ values and elevated $J_{red}(|\omega_H|-|\omega_N|)$ values. This anticorrelation is consistent with the theoretical expectation that the area bounded by $J(\omega)$ remains constant.

The description of the spectral densities as sums of Lorentzians centered on $\omega = 0$ appears qualitatively reasonable for eglin c. This is shown by the agreement between the analytical form for $J(\omega)$ given by Lipari and Szabo [$J_{ls}(\omega)$ in eq 17] and the experimental spectral density values. The monotonic decrease of $J_{red}(|\omega_H|-|\omega_N|)$ further corroborates that the description of the NH spectral densities in terms of a sum of Lorentzians centered at $\omega = 0$ is a viable one. Low $J_{eff}(0)$ values correlate with low-order parameters S^2. There are small but consistent deviations between the rate of decrease in $J(\omega)$ observed in experiment versus that predicted by $J_{ls}(\omega)$. In particular, $J_{ls}(\omega)$ predicts a faster and slower decrease in the neighborhood of ω_N and $|\omega_H| - |\omega_N|$, respectively. At the present, it cannot be distinguished whether this represents a true deviation of the experimental $J(\omega)$ values from $J_{ls}(\omega)$ or small systematic errors in experimental rate constants. This uncertainty is due partly to the use of presaturation in the relaxation experiments. Note that the use of more recent relaxation pulse sequences that exploit pulsed-field gradient methods would remove these uncertainties (Li & Montelione, 1994; Dayie & Wagner, 1994).

While the assumptions of the Lipari–Szabo formalism appear reasonable for eglin c, they may not be applicable for other systems. These would include, for example, molecules exhibiting correlations between internal degrees of freedom and overall molecular reorientation or systems lacking a single structured core. The ^{15}N dynamics study of the drkN SH3 domain by Farrow et al. (1995) is an example of the latter case. The attraction of the spectral density-mapping technique, then, is that it yields dynamics information without forcing one to adopt the assumptions of a specific motional model. In doing so, the approach does not replace the use of models. Instead, it simply provides the intrinsic dynamic information from the relaxation data, upon which a variety of motional models may be evaluated.

ACKNOWLEDGMENT

We are indebted to Dr. Markus Grütter and Dr. Dirk Heinz for the gift of ^{15}N eglin c and Mr. Kwaku Dayie, Dr. Jasna Fejzo, and Prof. Jean-François Lefévre for fruitful discussions. We thank Dr. Frank Laukien, Dr. Tom Kelley, and Dr. Aki Yamamoto of Bruker Instruments, Billerica, MA, for providing access to a 7.04 T magnet. We would also like to thank Dr. Dennis Hare for providing FELIX 2.05.

SUPPORTING INFORMATION AVAILABLE

Four tables containing the experimental relaxation rate constants at 7.04, 11.74, and 14.1 T; full spectral density values at 0, 30, 50, 60, 270, 300, 330, 450, 500, 550, 540, 600, and 660 MHz; reduced spectral density values at 0, 30, 50, 60, 270, 450, and 540 MHz; and the fitted values for S^2, τ_i, S_s^2, and S_f^2 (39 pages). Ordering information is given on any current masthead page.

REFERENCES

Abragam, A. (1961) *The Principles of Nuclear Magnetism*, Clarendon Press, Oxford, England.

Akke, M., Skelton, H. J., Kördel, J., Palmer, A. G., III, & Chazin, W. J. (1993) *Biochemistry 32*, 9832.

Allerhand, A., Doddrell, D., Glushko, V., Cochran, D. W., Wenkert, E., Lawson, P. J., & Gurd, F. R. N. (1971) *J. Am. Chem. Soc. 93*, 544–546.

Barbato, G., Ikura, M., Kay, L. E., Pastor, R. W., & Bax, A. (1992) *Biochemistry 31*, 5269–5278.

Bax, A., & Davis, D. (1985) *J. Magn. Reson. 65*, 355–360.

Bax, A., Ikura, M., Kay, L. E., Torchia, D. A., & Tschudin, R. (1990) *J. Magn. Reson. 86*, 304–318.

Bodenhausen, G., & Ruben, D. (1980) *Chem. Phys. Lett. 69*, 185.

Boyd, J., Hommel, U., & Campbell, I. D. (1990) *Chem. Phys. Lett. 175*, 477–482.

Braunschweiler, L., & Ernst, R. R. (1983) *J. Magn. Reson. 53*, 521–528.

Cheng, J.-W., Lepre, C. A., Chambers, S. P., Fulghum, J. R., & Moore, J. M. (1993) *Biochemistry 32*, 9000.

Cheng, J.-W., Lepre, C. A., & Moore, J. M. (1994) *Biochemistry 33*, 4093.

Clore, G. M., Szabo, A., Bax, A., Kay, L. E., Driscoll, P. C., & Gronenborn, A. M. (1990a) *J. Am. Chem. Soc. 112*, 4989–4991.

Clore, G. M., Driscoll, P. C., Wingfield, P. T., & Gronenborn, A. M. (1990b) *Biochemistry 29*, 7387–7401.

Dalvit, C. (1991) *J. Magn. Reson. 95*, 410–416.

Dalvit, C., & Bodenhausen, G. (1989) *Chem. Phys. Lett. 161*, 554.

Davis, D. G., Perlman, M. E., & London, R. E. (1994) *J. Magn. Reson. B104*, 266–275.

Dayie, K. T., & Wagner, G. (1994) *J. Magn. Reson. 111A*, 121–126.

Deverell, C., Morgan, R. E., & Strange, J. H. (1970) *Mol. Phys. 18*, 553–559.

Ernst, R. R., Bodenhausen, G., & Wokaun, A. (1987) *Principles of Nuclear Magnetic Resonance in One and Two Dimensions*, Oxford University Press, Oxford, England.

Farrow, N. A., Zhang, O., Forman-Kay, J. D., & Kay, L. E. (1995) *Biochemistry 34*, 868–878.

Fejzo, J., Westler, W. M., Macura, S., & Markley, J. L. (1991) *J. Magn. Reson. 92*, 20.

Gerald, R., II, Bernhard, T., Haeberlen, U., Rendell, J., & Opella, S. (1993) *J. Am. Chem. Soc. 115*, 777–782.

Goldman, M. (1988) *Quantum Description of High-Resolution NMR in Liquids*, Clarendon Press, Oxford, England.

Habazettl, J., & Wagner, G. (1995) *J. Magn. Reson. B109*, 100–104.

Heinz, D. W., Hyberts, S. G., Peng, J. W., Priestle, J. P., Wagner, G., & Grütter, M. G. (1992) *Biochemistry 31*, 8755–8766.

Hipler, K., Priestle, J. P., Rahuel, J., & Grütter, M. G. (1992) *FEBS Lett. 309*, 139–145.

Hiyama, Y., Niu, C., Silverton, J. V., Bavaso, A., & Torchia, D. A. (1988) *J. Am. Chem. Soc. 110*, 2378–2383.

Hyberts, S. G., & Wagner, G. (1990) *Biochemistry 29*, 1465–1474.

Hyberts, S. G., Goldberg, M. S., Havel, T. F., & Wagner, G. (1992) *Protein Sci. 1*, 736–751.

Jardetzky, O., & Roberts, G. C. K. (1981) *NMR in Molecular Biology*, Academic Press, New York.

Kay, L. E., Torchia, D. A., & Bax, A. (1989) *Biochemistry 28*, 8972–8979.

Kay, L. E., Nicholson, L. K., Delaglio, F., Bax, A., & Torchia, D. A. (1992) *J. Magn. Reson. 97*, 359.

Keiter, E. A. (1986) Ph.D. Thesis, University of Illinois.

Kelsh, L. P., Ellena, J. F., & Cafiso, D. S. (1992) *Biochemistry 31*, 5136–5144.

King, R., & Jardetzky, O. (1978) *J. Chem. Phys. Lett. 55*, 15–18.

Kinoshita, K., Kawato, W., Jr., & Ikegami, A. (1977) *Biophys. J. 20*, 289

Kördel, J., Skelton, N. J., Akke, M., Palmer, A. G., & Chazin, W. J. (1992) *Biochemistry 31*, 4856–4866.

Lefévre, J.-F., Dayie, K. T., Peng, J. W., & Wagner, G. (1996) *Biochemistry* (submitted for publication).

Li, Y. C., & Montelione, G. T. (1994) *J. Magn. Reson. 105B*, 45–51.

Lipari, G., & Szabo, A. (1982a) *J. Am. Chem. Soc. 104*, 4546–4559.

Lipari, G., & Szabo, A. (1982b) *J. Am. Chem. Soc. 104*, 4559–4570.

Marion, D., & Wüthrich, K. (1983) *Biochem. Biophys. Res. Commun. 113*, 967–974.

Märki, W., Rink, H., Schnebli, H. P., Liersch, M., Raschdorf, F., & Richter, W. (1985) in *Peptides: Structure and Function, Proceedings of the 9th American Peptide Symposium* (Deber, C. M., Hruby, V. J., & Kopple, K. D., Eds.) pp 385–388, Pierce Chemical Co., Rockford, IL.

Marquardt, D. W. (1963) *J. Soc. Ind. Appl. Math. 11*, 431–441.

McPhalen, C. A., & James, M. N. G. (1987) *Biochemistry 26*, 261–269.

McPhalen, C. A., & James, M. N. G. (1988) *Biochemistry 27*, 6582–6598.

McPhalen, C. A., Schnebli, H. P., & James, M. N. G. (1985) *FEBS Lett. 188*, 55–58.

Neuhaus, D., & van Mierlo, C. P. M. (1992) *J. Magn. Reson. 100*, 221.

Nicholson, L. K., Yamazaki, T., Torchia, D. A., Grzesiek, S., Bax, A., Stahl, S. J., Kaufman, J. D., Wingfield, P. T., Lam, P. Y. S., Jadhav, P. K., Hodge, C. N., Domaille, P. J., & Chang, C. H. (1995) *Nat. Struct. Biol. 2*, 274–280.

Nirmala, N. R., & Wagner, G. (1988) *J. Am. Chem. Soc. 110*, 7557–7558.

Nirmala, N. R., & Wagner, G. (1989) *J. Magn. Reson. 82*, 659–661.

Palmer, A. G., III, Skelton, N. J., Chazin, W. J., Wright, P. E., & Rance, M. (1991) *Mol. Phys. 75*, 699–711.

Peng, J. W., & Wagner, G. (1992a) *J. Magn. Reson. 98*, 308.

Peng, J. W., & Wagner, G. (1992b) *Biochemistry 31*, 8571–8586.

Peng, J. W., & Wagner, G. (1994a) *Methods Enzymol. 239*, 563–596.

Peng, J. W., & Wagner, G. (1994b) in *Nuclear Magnetic Resonance Probes of Molecular Dynamics* (Tycko, R., Ed.) pp 373–454, Kluwer Academic Publishers Dordrecht, The Netherlands.

Peng, J. W., Thanabal, V., & Wagner, G. (1991a) *J. Magn. Reson. 94*, 82–100.

Peng, J. W., Thanabal, V., & Wagner, G. (1991b) *J. Magn. Reson. 95*, 421–427.

Powers, R., Clore, G. M., Stahl, S. J., Wingfield, P. T., & Gronenborn, A. M. (1992) *Biochemistry 31*, 9150.

Press, W. H., Flannery, B. P., Teukolsky, S. A., & Vetterling, W. T. (1988) *Numerical Recipes in C - The Art of Scientific Computing*, Cambridge University Press, New York.

Redfield, A. G. (1957) *IBM J.*, 19–31.

Redfield, C., Boyd, J., Smith, L. J., Smith, A. R. G., & Dobson, C. M. (1992) *Biochemistry 31*, 10431.

Richarz, R., Nagayama, K., & Wüthrich, K. (1980) *Biochemistry 19*, 5189–5196.

Schleich, T., Morgan, C. F., & Caines, G. H. (1989) *Methods Enzymol. 176A*, 386–418.

Schneider, D. M., Dellwo, M. J., & Wand, A. J. (1992) *Biochemistry 31*, 3645–3652.

Shaka, A. J., Barker, P. B., & Freeman, R. (1985) *J. Magn. Reson. 64*, 547–552.

Slichter, C. P. (1978) *Principles of Magnetic Resonance*, Springer-Verlag, New York.

Stone, M. J., Chandrasekhar, K., Holmgren, A., Wright, P. E., & Dyson, H. J. (1993) *Biochemistry 32*, 426–435.

Szyperski, T., Luginbühl, P., Otting, G., Güntert, P., & Wüthrich, K. (1993) *J. Biol. NMR 3*, 151.

Wagner, G. (1994) Approaches for Studies of Protein Mobility and Structure, *The 35th Experimental Nuclear Magnetic Resonance Conference*, April 10–15, 1994, Asilolmar, CA.

Wennerström, H. (1972) *Mol. Phys. 24*, 69–80.

Wittebort, R. J., & Szabo, A. (1978) *J. Chem. Phys. 69*, 1723–1736.

Woessner, D. E. (1962) *J. Chem. Phys. 36*, 647–654.

BI951874E